






Inhomogeneous magnetic fields interacting with spinful states in a double quantum dot: Evidence for a staggered spin-orbit interaction

L. C. Contamin,¹ T. Cubaynes ¹, W. Legrand ¹, M. Marganska ², M. Villiers,¹ M. M. Desjardins,¹ M. C. Dartiailh,¹ V. Vinel ¹, Z. Leghtas,^{1,3,4} A. Thiaville,⁵ S. Rohart,⁵ A. Cottet,¹ M. R. Delbecq,^{1,*} and T. Kontos ^{1,*}

¹Laboratoire de Physique de l'École Normale Supérieure, ENS, Université PSL, CNRS, Sorbonne Université, Université Paris-Diderot, Sorbonne Paris Cité, Paris, France

²Institute for Theoretical Physics, University of Regensburg, 93040 Regensburg, Germany

³QUANTIC team, INRIA de Paris, Paris, France

⁴Centre Automatique et Systèmes, Mines-ParisTech, PSL Research University, Paris, France

⁵Laboratoire de Physique des Solides, Université Paris-Saclay, CNRS UMR 8502, Orsay, France



(Received 19 December 2021; revised 2 September 2022; accepted 24 January 2023; published 28 February 2023)

The coupling of the spin and the motion of charge carriers is an important ingredient for the manipulation of the spin degree of freedom and for the emergence of topological matter. Creating domain walls in the spin-orbit interaction at the nanoscale may turn out to be a crucial resource for engineering topological excitations suitable for universal topological quantum computing or for new schemes for spin quantum bits. Realizing this in natural platforms remains a challenge. Using circuit quantum electrodynamics magnetospectroscopy, we investigate the spinful states of a double quantum dot made in a single wall carbon nanotube with lithographically patterned magnetically textured gates. While a full understanding of the behavior of our magnetic textures would be helpful, the experimental signals are consistent with a change of the spin-orbital structure of the states above each gate. The coherence of the data, backed up by extensive theoretical modeling and a control device, points towards the existence of a synthetic staggered spin-orbit interaction in our device.

DOI: [10.1103/PhysRevB.107.085152](https://doi.org/10.1103/PhysRevB.107.085152)

I. INTRODUCTION

Mastering spin-orbit interaction at the nanoscale is an important topic of condensed matter research which has turned out to be crucial for the emergence of topological excitations. Many recent studies in materials with *a priori* strong spin-orbit interaction such as semiconducting nanowires question whether the requirements for topological superconductivity large spin orbit, superconductivity, and large magnetic Zeeman splitting can be met together [1,2]. Many theoretical works have suggested an alternative route in an all proximity platform which consists essentially of proximity magnetic textures and proximity superconductivity. As a first important step, we have constructed an elementary two site chain which shows the basic requirements needed for a chain, i.e., that one can change its local parameters, and importantly, its local spin-orbit interaction by an amount larger than the hopping between the sites. In view of the scalability of our approach, we can envision to build, besides engineering exotic electronic states [3,4], longer chains of 10 to 20 sites which could host non-Abelian excitations.

Such a setup can readily be implemented using a double quantum dot (DQD) and the corresponding matrix element can directly be measured by cavity quantum electrodynamics techniques [5]. The large electric field gradients which can be achieved inside a microwave cavity enable the sensing

of magnetically active nanoscale dipoles [6]. Specifically, we study a device made out of a carbon nanotube double quantum dot proximal to two different magnetic textures inducing locally different synthetic spin-orbit interactions [7]. As a consequence, the localized energy levels respond differently to the external magnetic field. The microwave signal reveals a large difference of the magnetic field response of the two dots, witnessing a large spin-orbit contrast at the nanoscale.

The principle of our experiment is depicted in Fig. 1(a). A double quantum dot with each of the two dots subject to two different synthetic spin-orbit interactions is coupled to a photonic field which actuates tunneling between these two dots as schematized by the orange arrow [8]. The electric dipole ϕ stems from tunneling between the two dots which is directly linked to the overlap between the wave functions of the left and the right dots. Owing to the band structure of carbon nanotubes, the single-particle Hilbert space has at least four dimensions for each of the two dots due to the spin and the orbital degeneracies.

II. EXPERIMENTAL SETUP

Our physical implementation of such a setup is presented in Fig. 1(b). A double quantum dot is formed in a single wall carbon nanotube (CNT) using a nanoassembly technique [9]. The device is designed with two magnetically textured gates, colored in blue in Fig. 1(b), made out of CoPt stacks [7] above which the nanotube is transferred. From the magnetic force microscope (MFM) micrograph shown in Fig. 1(c),

*These authors cosupervised this work

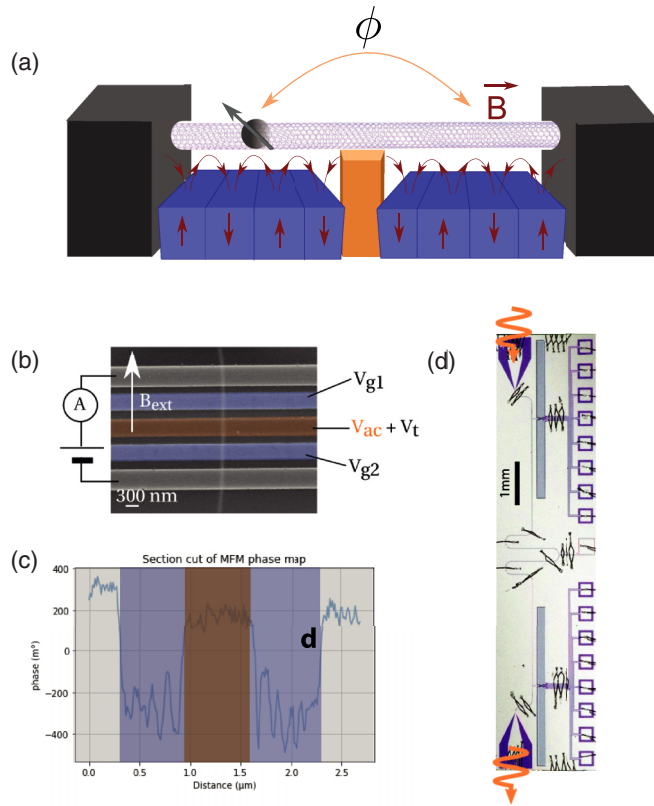


FIG. 1. The device. (a) Schematics of the DQD. It is defined inside a CNT connected to two normal contacts (grey). The two blue gates yield an oscillating magnetic field (red) at the level of the dots. The DQD is also coupled to a microwave cavity through the orange gate; as a consequence, the transmission phase Φ is sensitive to the charge susceptibility of the DQD. (b) False-color SEM image of the sample, with the CNT highlighted in white. The central orange gate is connected to the cavity central conductor. The two lateral blue gates are made of the CoPt stacks. (c) MFM phase cut of the sample, displaying oscillations of the AFM phase signal above the magnetic gates (blue region). (d) Photograph of the CPW resonator in which the sample is embedded.

modulations of the magnetic signal are observed with a length scale λ of about 170 nm for the left dot and 150 nm for the right dot. This yields *a priori* a large and inhomogeneous spin-orbit energy scale [8,10] of $h v_F / 2\lambda \approx 8$ meV, where v_F is the Fermi velocity in the SWNT, comparable to the mean energy level spacing of each dot, of about $h v_F / 2L \approx 3$ meV, where $L \approx 500$ nm is the designed physical length of each dot. The device is embedded in a Nb microwave cavity with a quality factor of about 1000 and a resonance frequency of $f_{\text{cav}} = 6.42$ GHz, shown in Fig. 1(d).

The two devices presented here consist in DQD made out of a CNT, stapled over a mesoscopic circuit using the stapling technique described in Ref. [9]. The DQD is coupled to a $\lambda/2$ coplanar waveguide (CPW) resonator etched from a Nb thin film.

We now describe in more details the fabrication and measurement techniques. The electrical circuit and microwave cavity were lithographically defined on a high-resistivity Si/SiO₂ substrate. First, a 100-nm-thick Nb layer is

evaporated at a pressure below 5×10^{-10} mbar, then the cavity pattern is defined with laser lithography and etched using a reactive ion etching (RIE) process with SF₆. The CPW resonator of sample 2 is represented in Fig. 1(d). Then, the nanoscale circuit for defining the DQD is drawn using electron beam lithography and metal evaporation processes. Trenches are defined around this circuit with either optical or electron beam lithography and RIE etching. Carbon nanotubes were chemically grown using a methane process, on a separated chip designed for the nanoassembly process, and subsequently transferred under vacuum. Once a good electrical contact is measured at room temperature, the circuit is transferred to a cryostat. The nanoassembly step occurs after all the nanolithography steps, including the deposition of the magnetic gates.

Both samples were characterized in a dilution fridge with base temperature of about 20 mK, through simultaneous DC and RF measurements. For RF measurement, a heterodyne detection scheme is used with a modulation frequency of 20 MHz. For every change in magnetic field, the change in the bare cavity resonant frequency is measured with the DQD transitions detuned.

The two devices differ in the nanoscale circuit defining the DQD. For the main device, the CNT is positioned over two magnetically textured gates and a central Al/AIOx gate. This last gate can be DC biased and is also connected to the central conductor of the microwave cavity. The magnetic gates are made out of ten repetitions of Co/Pt, with a Ta/Pt initial layer and a thin AlOx cap. The CNT is connected to two Pd electrodes, through which a current can be measured. The electrode height is chosen so that the CNT is lying on the magnetic gates, to maximize their effect.

The control device on the other hand, was fabricated with several Al/AIOx gates and two narrow magnetic gates with only five repetitions of a Pt/Co bilayer. The CNT is again connected with two Pd contacts. The electrode height is increased, so that the CNT is suspended above the gate structure (as in Ref. [9]). The CNT is capacitively coupled to a microwave cavity through one of the Al/AIOx gates, of resonant frequency 6.439 GHz and quality factor 1600.

III. CAVITY BASED MAGNETOSPECTROSCOPY

The phase of the cavity transmission is sensitive to the charge susceptibility of the quantum circuit [11]. Such measurements are presented in Figs. 2(a) and 2(b) for the control and the textured device, respectively. The charge susceptibility is mainly sensitive to interdot tunneling but also, weakly to the dot-lead tunneling [11]. In both cases, we see qualitatively the same features. On the top of a faintly visible “honeycomb” pattern characteristic of the stability diagram of a double quantum dot, we see, as expected, large phase contrasts of about 10° – 20° at the interdot tunneling edge. On each of panels a and b an arrow is superimposed, indicating the “detuning” axis between the left and right dot of the corresponding gate voltage setting. The E_d label corresponds to the detuning.

We discuss now how we convert in energy the detuning axis. A first approximative value for the lever arms of both gates was extracted from Coulomb diamonds. However, the

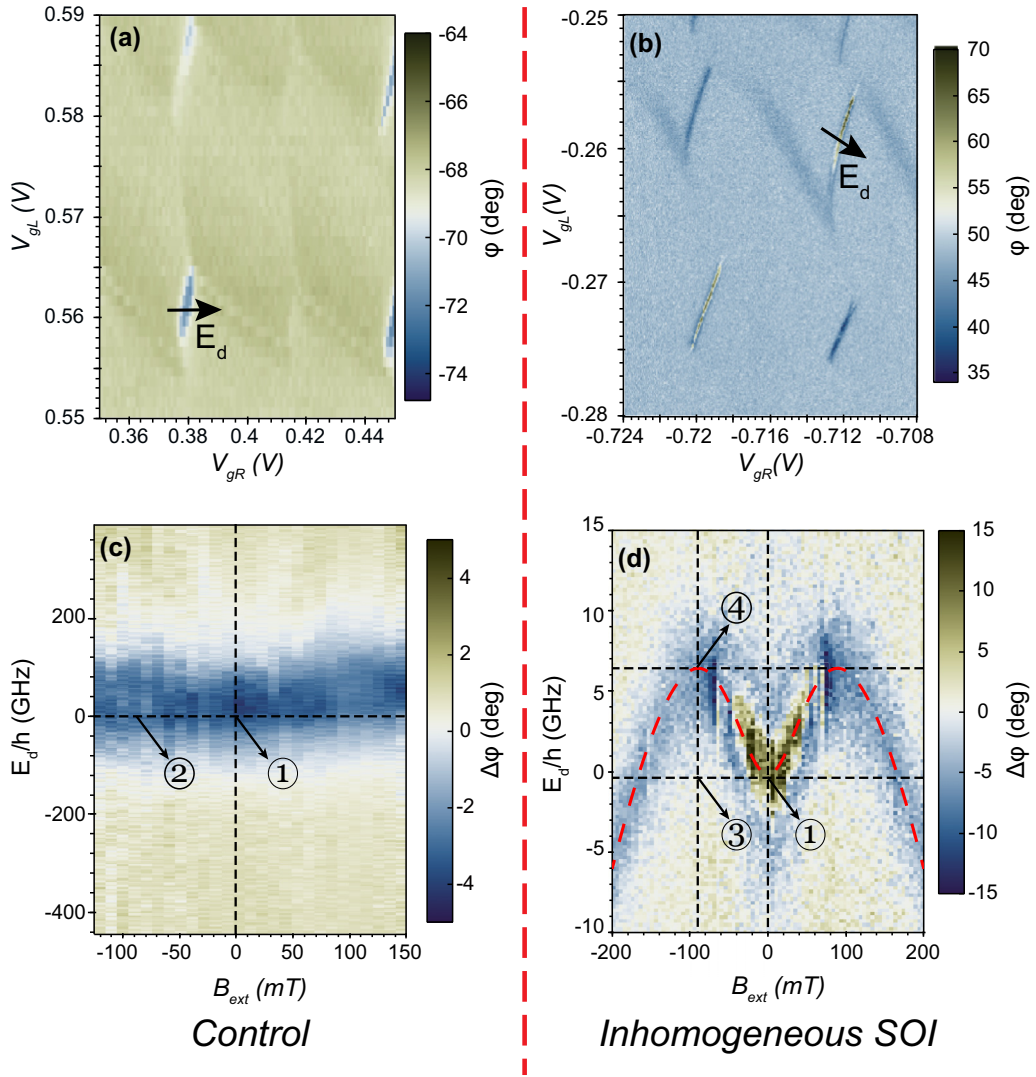


FIG. 2. Magnetospectroscopy of staggered and control device. [(a) and (b)] V_{gR} - V_{gL} cavity phase shift maps for the control (a) and main (b) samples. [(c) and (d)] B_{ext} - E_d maps of the cavity phase shift, over a magnetic field range of about $\pm(0.15 - 0.2)$ T for the two samples and along the E_d cut shown by a black arrow in the respective (a) and (b). For the control sample (c), the cavity signal is unaffected by the external magnetic field, as opposed to the main sample (d). Circled numbers refer to situations described in Fig. 3(a). The red dashed lines are a fit to the transition energy with the simplified model.

strong interdot coupling deforms the stability diagram and hinders a precise measurement of these lever arms. A correction to the lever arms is thus kept as a general parameter in order to compare with our models. First, the gate voltages are converted into a detuning value for the main sample through

$$E_d = \mu_R - \mu_L \text{ with } \mu_R = 0.31V_{gR} - 0.025V_{gL}$$

$$\text{and } \mu_L = -0.10V_{gR} + 0.11V_{gL}.$$

We anticipate now on our fitting of the microwave measurements. Fitting the interdot transition cavity phase shift at zero external magnetic field imposes strong constraints on the energy axis and thus acts as a self calibration. The electronic temperature and the interdot tunneling affect very differently the shape of the phase contrast. The electronic temperature affects more the amplitude of the phase contrast while the

interdot tunneling affects more its width. They can therefore to a large extent be considered as evaluated separately although they are calibrated in a single step. We find that all interdot transitions signals can be quantitatively reproduced by applying a factor 1/4 to E_d which is then fixed to this value in all analysis. The width is essentially fitted for getting the factor 1/4. It is therefore mainly the interdot tunneling which sets this procedure. The values of the fitting parameters of the different interdot transitions are given below as well as details of data and fits of each subpanel of Fig. 10. The gate voltages to detuning conversion factor for the control sample are comparable to the ones of the main sample and given by

$$E_d = \mu_R - \mu_L \text{ with } \mu_R = 0.33V_{gR} - 0.1V_{gL}$$

$$\text{and } \mu_L = -0.16V_{gR} + 0.621V_{gL}.$$

The magnetic field dependence of the phase contrast along each of the arrows allows one to map the spin-orbit dependence of the energy levels of the double quantum dots. Such a map is displayed in Figs. 2(c) and 2(d) for the control as well as for the staggered device. The control device map is shown in Fig. 2(c). As shown in the Appendix, the control device has three nonmagnetic gates above which the double quantum dot is formed and two Co/Pt magnetic gates. The MFM signal above each of these gates is markedly different from the one shown in Fig. 1(c). No modulation is observed above the CoPt electrodes indicating essentially a single domain structure on the lateral scale of the magnetic gate. Such a control device has therefore all the elements present in the staggered one but without the magnetic modulation observed in Fig. 1(c). The phase contrast as a function of $V_{gR} - B_{ext}$ over the values spanned by the black arrow is shown in Fig. 2(c). Up to a faint “upturn” on the right hand side due to a non reproducible gate drift, the cavity signal at resonance does not change with an external magnetic field between ± 150 mT. Like for any gated devices, there are charges trapped on the substrate in the vicinity of the gates and of the quantum dots. They fluctuate over time and usually lead to abrupt jumps in the 2D maps. There are some instances where they change gradually the electrostatic background, which typically leads to the “faint upturn” mentioned above. These changes are not reproducible and qualitatively different from the stable and reproducible maps for the main device of the manuscript. A very different signal is observed for the staggered sample as shown in Fig. 2(d). The phase contrast resonance starts to shift towards positive detuning up to 10 GHz at ± 100 mT and then shifts towards negative detuning values down to -5 GHz. This occurs symmetrically for positive and negative magnetic field.

The phenomenology of the above findings can be captured through the cartoon picture of Fig. 3. In a double-quantum dot setup, a phase shift is measured when two energy levels are essentially resonant, as sketched in the leftmost panel (1) of Fig. 3(a). When an external magnetic field is applied, $B_{ext} \neq 0$, the energy levels are shifted by an energy $\delta E_{L(R)} = g_{L(R)} \mu_B B_{ext}$, where $g_{L(R)}$ is an *effective* Landé factor in the left (right) dot. In absence of a magnetic texture, the two dots being formed inside the same CNT, the Landé factor is expected to be identical in the two dots and $\delta E_L = \delta E_R$ as shown in panel (2) of Fig. 3(a). In this situation, the cavity signal at the resonant frequency is expected to be unaffected by the external magnetic field (the linewidth of the cavity is not affected much at these magnetic fields). This is what happens in the control device. In contrast, in the second situation where $g_L \neq g_R$, as illustrated in panels (3) and (4) of Fig. 3(a), one has to apply a finite detuning E_d in order to bring two spinful levels in resonance. This leads to a dispersion of the interdot phase resonance in the $E_d - B_{ext}$ plane. This is what happens in the staggered device. The reason for having a very inhomogeneous Landé factor between the left and the right dot can be captured in the cartoon pictures of Figs. 3(b) and 3(c). First, each wave function has a different overlap with the magnetic texture as shown in Fig. 3(b). Second, these different overlaps change as a function of the magnetic field quite strongly because a small magnetic field changes the domain structure of the magnetic texture. Hence, we can qualitatively

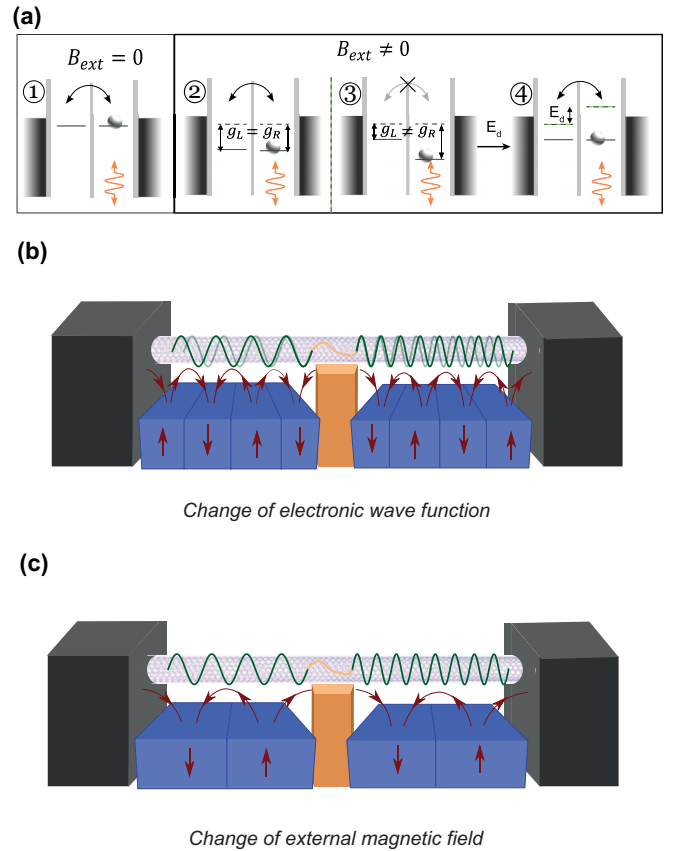


FIG. 3. Picture of evolution of DQD levels and of the staggered spin-orbit interaction. (a) Schematic representation of the evolution of the DQD charge susceptibility with an external field B_{ext} , from a no-detuning situation [panel (1)]. When the left and right Landé factors are equal, $g_L = g_R$, the cavity signal is unaffected by B_{ext} [panel (2)]. When they are different, the cavity signal is modified [panel (3)], but the resonant condition can be recovered with a finite detuning E_d [panel (4)]. (b) Schematic illustrating the evolution of the spinful levels resulting from the overlap between the electronic wave function and the magnetic textures stray field due to a change of gate configuration. (c) Schematic illustrating the evolution of the spinful levels resulting from the overlap between the electronic wave function and the magnetic textures stray field due to a change of external magnetic field.

conclude that the findings presented in Fig. 2(d) are strongly suggestive of a staggered spin-orbit interaction.

IV. THEORY OF A SYNTHETIC SPIN-ORBIT INTERACTION IN A SINGLE WALL CARBON NANOTUBE

The simplest model we use to account for the very large g -factors measured above is a simple two level system model (spin qubit). It is very appealing since it is very simple. It is however not obvious that the level structure will be the same in the actual system. This is why we develop in this section models with growing complexity, up to a full model treating explicitly the carbon nanotube band structure. We then first develop a low-energy theory using a Schrieffer-Wolf transformation on the nanotube Dirac Hamiltonian taking into account the intrinsic spin-orbit interaction of nanotubes and

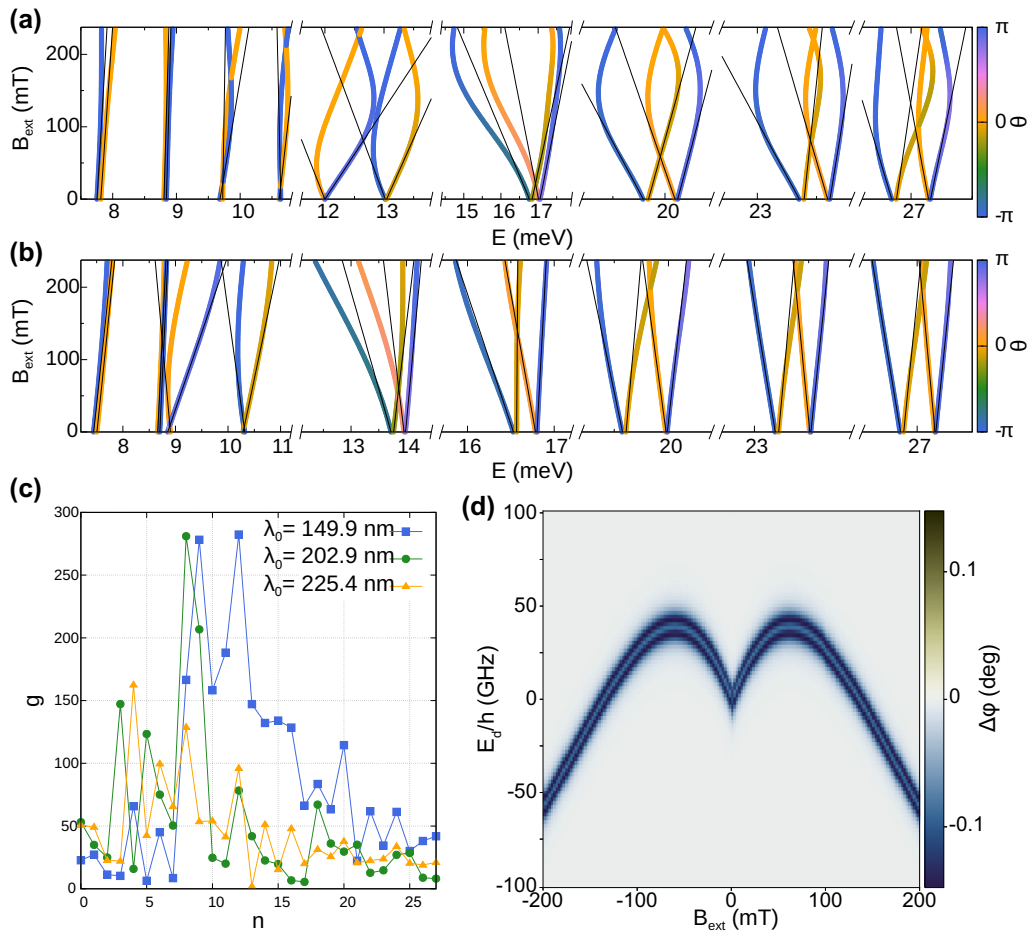


FIG. 4. Numerics for the spectrum of a carbon nanotube with magnetically textured gates. (a) Spectrum of a carbon nanotube with periods $\lambda_0 = 225.4$ nm as a function of the external magnetic field B_{ext} . (b) Spectrum of a carbon nanotube with periods $\lambda_0 = 149.9$ nm as a function of the external magnetic field B_{ext} . (c) Effective Landé factors resulting from the magnetic texture for three different texture periods. (d) Calculated microwave phase signal using the numerical spectrum. The magnetic field dependence of the input energy levels has been symmetrized, consistently with the experiment. The energy levels correspond to an electron filling $n1 = 11$ for the left dot and $n2 = 23$ for the right dot.

the K/K' valleys. This yields Hamiltonian (8), (9) which is not a two level system but produces the same spectrum as that of the spin qubit for the two lowest levels. Then, we go to real space modeling to further justify the structure of Hamiltonian (8), (9), which was produced by perturbation theory on the Dirac Hamiltonian. This layer of modeling treats the full band structure of nanotubes and its dependence upon changes in the parameters (e.g., B field and magnetic texture) of the experimental system. The spectrum and the eigenstates of electrons in a finite sized carbon nanotube subject to a cycloidal magnetic field in the general case is *a priori* complex. We obtain it in two ways: both by an analytical calculation in the reciprocal space and a numerical tight-binding simulation on the atomic lattice (see below and the Appendix). Both approaches agree very well, and the analytical one yields the low-energy Hamiltonian (8), (9). As shown in Figs. 4(a) and 4(b) for two different initial periods λ_0 of the cycloidal field, 149.9 [Fig. 4(a)] and 225.4 nm [Fig. 4(b)], the cycloidal field produces very large slopes of the carbon nanotube energies in external magnetic field which, as shown in Fig. 4(c), yield very large effective Landé factors, up to about 280. Here, as assumed in a previous work [7], the large effective Landé

factor stems from the large spin polarization induced by the magnetic texture as well as the strong dependence of λ on the external field B_{ext} . One can insert the obtained spectra into the expected expression of the phase signal for a DQD. This yields the phase map of Fig. 4(d), which is qualitatively similar to that of Fig. 2(d). Note that the B_{ext} dependence of the magnetic parameters of the numerics has been assumed to be symmetric with respect to B_{ext} direction to make contact with the experimental findings (see the Appendix). It is important to add here that this is not at all the case for the spin qubit model which we use for accounting for the measurements of Fig. 10 where the magnetic field symmetry is naturally present in the theory.

A. Local fields and effective- g model

We assume here that the Hamiltonian of the system can be simplified if one considers the ground state and the first excited state. This is fully justified in our case since the cavity is energy selective and filters the transition which is the closest to the cavity frequency $\omega_{\text{cav}}/2\pi$. We therefore model our devices as a double quantum dot (DQD) with one level in each

dot, with an effective spin degree of freedom corresponding to the ground and excited states of Hamiltonian (8) and (9).

The two ground state levels are detuned by an energy E_d , and coupled through a tunnel coupling of energy t . We introduce $\rho_{0,x,y,z}$, $\pi_{0,x,y,z}$ as the Pauli matrices for the left/right and effective spin subspaces. Each dot is subject to a local effective field $B_{L,R}$ that is in the $x - y$ plane (B_L is along the x axis, and B_R has an angle θ to B_L). An external magnetic field B_{ext} can be applied along the z axis, that is the axis of the CNT. B_{ext} can thus both have a Zeeman and orbital contribution to the spectrum. The orthogonality between B_{ext} and the local effective field ensures a symmetric spectrum with respect to B_{ext} , as experimentally observed.

The model Hamiltonian is the following:

$$H_{\text{tot}} = \frac{E_d}{2} \rho_z + t \rho_x + H_{\text{spin},L} + H_{\text{spin},R}$$

with

$$H_{\text{spin},L} = -\frac{g_L \mu_B B_L}{4} (\rho_0 + \rho_z) \pi_x - \frac{g_L \mu_B B_{\text{ext}}}{4} (\rho_0 + \rho_z) \pi_z,$$

$$H_{\text{spin},R} = -\frac{g_R \mu_B B_R}{4} (\rho_0 - \rho_z) (\sin(\theta) \pi_x + \cos(\theta) \pi_y)$$

$$- \frac{g_R \mu_B B_{\text{ext}}}{4} (\rho_0 - \rho_z) \pi_z.$$

The cavity transmission is given by

$$T = \frac{\kappa/2}{(f_{\text{cav}} - f_d) - i\kappa/2 - \chi}, \quad (1)$$

where f_{cav} , κ are the cavity resonance frequency and line width and f_d is the drive frequency. The charge susceptibility χ is given by

$$\chi = \sum_{i,j} \chi_{ij} (n_i - n_j) \text{ and } \chi_{ij} = \frac{g_{ij}^2}{f_{ij} - f_d - i(\Gamma_1 + \Gamma_\phi/2)/2}, \quad (2)$$

with n_i , n_j the thermal occupations at an electronic temperature T_e , and $f_{ij} = f_i - f_j$ the transition frequency between eigenvalues i and j . The electron-photon coupling strength g_{ij} is calculated from the electron-photon coupling operator: $g_{ij} = g_0 |\langle i | \rho_0 - \rho_z | j \rangle| / 2$, where g_0 is a fit parameter. For simplicity, the dephasing rate $\Gamma_1 = 1$ MHz is kept constant, whereas the Γ_ϕ for each (i, j) are calculated from the model Hamiltonian H_{tot} (defined above) through the projection of the different dephasing operators with the initial and final states. The dephasing operators are ρ_z (charge) and π_z (spin).

B. Low-energy Hamiltonian of a carbon nanotube in the presence of a magnetic texture

We present in this section the derivation of the low-energy Hamiltonian of a single wall carbon nanotube in the presence

of a magnetic texture. The spectrum of the SWNT subject to an external magnetic field reads [12]

$$E_{\kappa,k,\tau,\sigma} = \pm \hbar v_F \sqrt{\kappa^2 + k^2} + \frac{1}{2} g_{\text{orb}} B_{\parallel} \tau + \frac{1}{2} g_s B_{\text{ext}} \sigma, \quad (3)$$

where $g_{\text{orb}(s)}$ are the orbital (spin) Landé factors, v_F the Fermi velocity, $\tau(\sigma)$ are the orbital (spin) indices, κ and k are the transverse and longitudinal wave vectors of the nanotube, respectively. Using the conventional quantization conditions for both κ and k , we can introduce the wave functions of electrons/holes in a quantum dot made out of a carbon nanotube:

$$\langle \varphi, \zeta | \Psi_{m,n,\tau,\sigma} \rangle = \frac{e^{i \vec{K}(\cdot) \cdot \vec{r}}}{\sqrt{4\pi}} e^{i(m-\tau\nu/3)\varphi} \Phi_{m,n}(\zeta), \quad (4)$$

where n and m are the quantum numbers for the transverse and longitudinal quantization, respectively. The parameter $\nu = 0, \pm 1$ encodes whether the nanotube is semiconducting ($\nu = \pm 1$) or metallic ($\nu = 0$). The wave function $\Phi_{m,n}(\zeta)$ has the usual spinor structure to account for the graphene sublattices [12]:

$$\Phi_{m,n}(\zeta) = C \begin{bmatrix} z_{\kappa_m, k_n, \tau} \\ 1 \end{bmatrix} e^{i k_n \zeta} + D \begin{bmatrix} z_{\kappa_m, -k_n, \tau} \\ 1 \end{bmatrix} e^{-i k_n \zeta} \quad (5)$$

with $z_{\kappa,k,\tau} = \pm \tau (\kappa - i\tau k) / \sqrt{\kappa^2 + k^2}$. The coefficients C and D depend on the boundary conditions of the nanotube. We would like to calculate the matrix elements arising from the spin texture. The corresponding terms in the nanotube Hamiltonian read [13]

$$\text{spin} : \frac{1}{2} g_s B_{\text{osc}} (\hat{\sigma}_z \cos 2\pi \zeta / \lambda + \hat{\sigma}_x \sin 2\pi \zeta / \lambda), \quad (6)$$

$$\text{valley} : \frac{1}{2} g_{\text{orb}} B_{\text{osc}} \hat{\tau}_z \hat{\eta}_x \cos 2\pi \zeta / \lambda. \quad (7)$$

In the above expressions, we have assumed a cycloidal magnetic texture oscillating with a period λ and an amplitude B_{osc} . The matrices $\hat{\sigma}_i$, $\hat{\tau}_i$, and $\hat{\eta}_i$ are the Pauli matrices acting on the spin, valley, and sublattice spaces, respectively. We define $k_\lambda = 2\pi / \lambda$. The matrix elements of these terms for the wave functions $|\Psi_{m,n,\tau,\sigma}\rangle$ are all of the form

$$\mathcal{A}_{mnm'} \frac{\sin((k_n \pm k_{n'} \pm k_\lambda)L/2)}{(k_n \pm k_{n'} \pm k_\lambda)L/2},$$

where L is the length of the confined region of the nanotube forming the quantum dot (assuming a square potential for the sake of simplicity) and $\mathcal{A}_{mnm'}$ is a coefficient which depends on the overlap between the wave functions of the dot and the subband index. We would like now to obtain an effective spin-valley Hamiltonian for the CNT. Two terms arise from the above discussion: terms which conserve the longitudinal index (first order) and terms which couple different orbitals. The Hamiltonian of the system is now:

$$H = \sum_n |n\rangle \langle n| \left[E_n + \frac{1}{2} g_s \mu_B (B_{\text{ext}} + \alpha_{nm}^{\sigma_z} B_{\text{osc}} \hat{\sigma}_z + \alpha_{nm}^{\sigma_x} B_{\text{osc}} \hat{\sigma}_x) + \frac{1}{2} g_{\text{orb}} \mu_B (B_{\text{ext}} + \beta_{nm}^{\tau_z} B_{\text{osc}}) \hat{\tau}_z \right] \quad (8)$$

$$+ \sum_{m'm} |n\rangle \langle n'| \left[\frac{1}{2} g_s \mu_B B_{\text{osc}} (\alpha_{m'n}^{\sigma_z} \hat{\sigma}_z + \alpha_{m'n}^{\sigma_x} \hat{\sigma}_x) + \frac{1}{2} g_{\text{orb}} \mu_B B_{\text{osc}} \beta_{m'n}^{\tau_z} \hat{\tau}_z \right] + \text{H.c.} \quad (9)$$

The second line terms modify at the second order the Hamiltonian. This can be calculated using a Schrieffer-Wolff transformation:

$$\tilde{H} = e^S H e^{-S} \approx H + [S, H] + \frac{1}{2}[S, [S, H]] + \dots$$

where S is a anti-Hermitian operator. The operator S has to be chosen such that its commutator with the diagonal part of the Hamiltonian in the orbital subspace (8) is exactly the opposite of the off-diagonal part (7). One can show that an operator satisfying these conditions has the following matrix elements:

$$\langle n, \sigma, \tau | S | m, \sigma', \tau' \rangle = \frac{[\sigma \delta_{\sigma\sigma'} \alpha_{nm}^{\sigma_z} + \sigma \delta_{\sigma\sigma'} \alpha_{nm}^{\sigma_x} + \tau \beta_{nm}^{\tau_z}] \delta_{\tau\tau'}}{E_n - E_m + \frac{1}{2} g_s \mu_B (B_{\text{ext}} + B_{\text{osc}} \sqrt{\alpha_{nm}^{\sigma_z^2} + \alpha_{nm}^{\sigma_x^2}}) \sigma - \frac{1}{2} g_s \mu_B (B_{\text{ext}} + B_{\text{osc}} \sqrt{\alpha_{nm}^{\sigma_z^2} + \alpha_{nm}^{\sigma_x^2}}) \sigma'},$$

where σ is the new quantum number along the quantization axis defined by the external field and the first-order terms of the magnetic field arising from the magnetic texture. Noting $E_{\text{SO}} = \hbar v_F / \lambda$, the final version of the Hamiltonian (projected on the orbital $|n\rangle$) is

$$H_{\text{eff}} = E_n + \frac{1}{2} g_s \mu_B (B_{\text{ext}} + \alpha_{nm}^{\sigma_z} B_{\text{osc}} \hat{\sigma}_z + \alpha_{nm}^{\sigma_x} B_{\text{osc}} \hat{\sigma}_x) + \frac{1}{2} g_{\text{orb}} \mu_B (B_{\text{ext}} + \beta_{nm}^{\tau_z} B_{\text{osc}}) \hat{\tau}_z \quad (10)$$

$$+ \gamma_{nm}^{\sigma_z \tau_z} \frac{g_s g_{\text{orb}} (\mu_B B_{\text{osc}})^2}{E_{\text{SO}}} \hat{\sigma}_z \hat{\tau}_z + \gamma_{nm}^{\sigma_x \tau_z} \frac{g_s g_{\text{orb}} (\mu_B B_{\text{osc}})^2}{E_{\text{SO}}} \hat{\sigma}_x \hat{\tau}_z + \gamma_{nm}^{\sigma_y} \frac{(g_s \mu_B B_{\text{osc}})^2}{E_{\text{SO}}} \hat{\sigma}_y + \frac{\gamma_{nm}^{\sigma_0} g_s + \gamma_{nm}^{\tau_0} g_{\text{orb}}}{E_{\text{SO}}} (\mu_B B_{\text{osc}})^2. \quad (11)$$

The dimensionless parameters $\alpha_{nm}^{\sigma_z}$, $\alpha_{nm}^{\sigma_x}$, $\beta_{nm}^{\tau_z}$, $\gamma_{nm}^{\sigma_0}$, $\gamma_{nm}^{\tau_0}$, $\gamma_{nm}^{\sigma_x \tau_z}$, $\gamma_{nm}^{\sigma_z \tau_z}$, and $\gamma_{nm}^{\sigma_y}$ are of the order of 1 and depend on the wave function, the value of λ and therefore on the external magnetic field B_{ext} as well. Their expressions are given in Sec. IV E. It is important to realize that we obtain for the two first terms of the second line the same form as that for the intrinsic spin-orbit interaction [14] in carbon nanotubes which shows that the magnetic texture plays indeed the role of an effective spin-orbit interaction. Finally, it is essential to note that the synthetic spin-orbit interaction acts already at first order as an effective magnetic field which depends on the wave functions through the parameters $\alpha_{nm}^{\sigma_z}$, $\alpha_{nm}^{\sigma_x}$, and $\beta_{nm}^{\tau_z}$ which imply in particular an orbital dependent effective field direction for the spin defined by the angle $\theta_n = \arctan[\alpha_{nm}^{\sigma_x} / \alpha_{nm}^{\sigma_z}]$.

We would like now to discuss the assumptions made on the magnetic texture here. At the beginning of this section, we have assumed that the magnetic texture had a perfect cosine like cycloidal shape. This is just for getting more intuitive calculations and for showing what length scales matter in the problem. As shown in formulas just above, the dimensionless parameters entering the effective Hamiltonian do not depend on that. They are just matrix elements from two orbital wave functions. Physically, this means that the structure of the low-energy Hamiltonian does not depend on the exact shape of both the wave functions and the magnetic texture but rather on the overlap between them, as sketched in Fig. 3. This stems from the fact that the orbital wave functions are 0D essentially. As a consequence, a perfect periodic texture is not needed in order to get a staggered spin-orbit interaction in our setup, which is a considerable experimental simplification. Note also that we do not need to make any assumption on the exact shape of the wave functions and their confinement potential for the general shape of the low-energy Hamiltonian.

C. Real space modelling

The tight-binding Hamiltonian is constructed for one p_z orbital per site,

$$H = \sum_{\langle i, j \rangle} \sum_{ss'} t_{ij,ss'}(\mathbf{B}) c_{is}^\dagger c_{js'} + \sum_{i,s} \mu_B [s B_{z,i} c_{is}^\dagger c_{is} + B_{x,i} c_{i,s}^\dagger c_{i,-s}] + \text{H.c.} \quad (12)$$

The first sum runs over the nearest-neighbor atomic positions $\langle i, j \rangle$ and contains the information about the intrinsic spin-orbit coupling and the orbital response to the magnetic field, the second sum accounts for the Zeeman effect, with $B_{\mu,i}$ the μ component of the magnetic field at the atom i . Without the magnetic field the hopping elements $t_{ij,ss'}$ from atom j to atom i are given by [15–17]

$$t_{ij,ss}(\mathbf{B} = 0) = V_{pp}^\pi \cos(\varphi_i - \varphi_j) - (V_{pp}^\sigma - V_{pp}^\pi) \times \frac{R^2}{a_c^2} [1 - \cos(\varphi_i - \varphi_j)]^2 + s 2i \delta_{\text{SO}} \{ V_{pp}^\pi \sin(\varphi_i - \varphi_j) + (V_{pp}^\sigma - V_{pp}^\pi) \times \frac{R^2}{a_c^2} \sin(\varphi_i - \varphi_j) [1 - \cos(\varphi_i - \varphi_j)] \}, \quad (13)$$

$$t_{ij,s,-s} = -s \delta_{\text{SO}} (V_{pp}^\sigma - V_{pp}^\pi) \frac{R(z_i - z_j)}{a_c^2} \times [1 - \cos(\varphi_i - \varphi_j)] (e^{i\varphi_i} + e^{i\varphi_j}), \quad (14)$$

where s is the electron spin, R the nanotube radius, $a_c = 1.42$ Å the carbon-carbon bond length, and φ_i and z_i the polar and axial coordinates of the i th atom. The hopping integrals

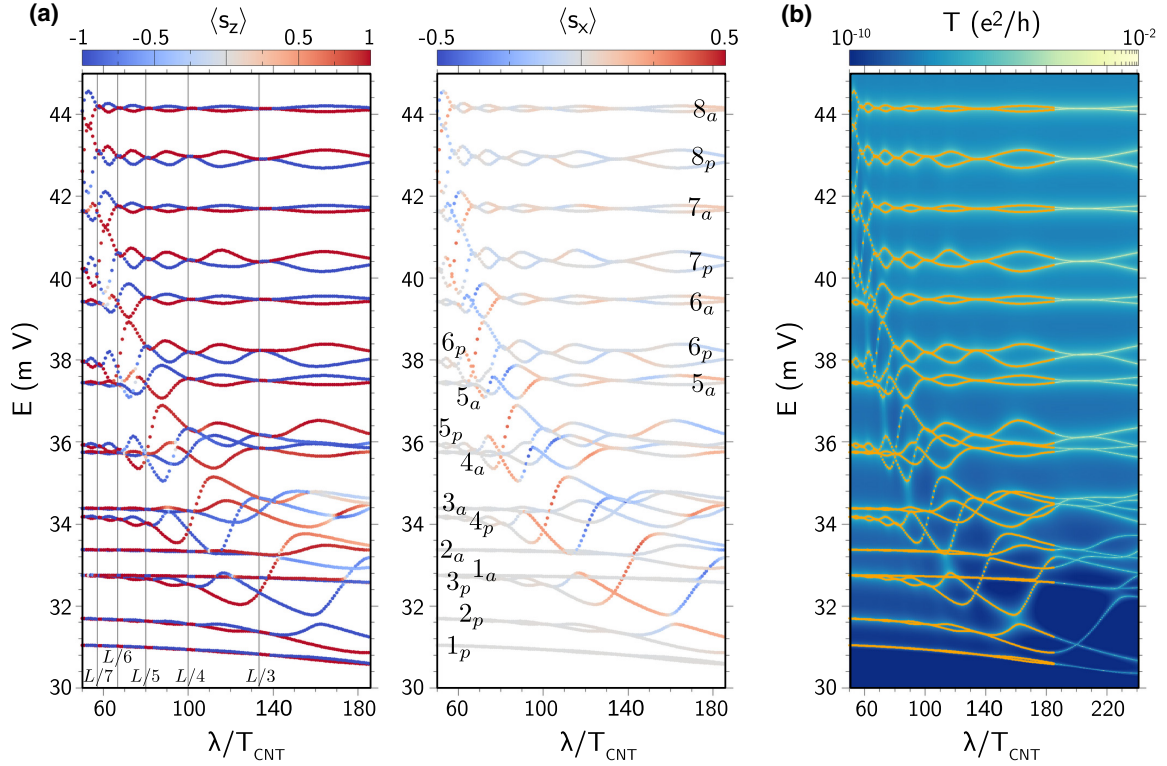


FIG. 5. Spectrum of a $(6, 3) \times 400$ CNT ($d = 0.62$ nm, $L = 451$ nm) in cycloidal magnetic field with $B_{\text{osc}} = 10$ T and $\delta = 0$, as a function of the magnetic period λ . (a) Energy levels and spin expectation values $\langle s_z \rangle$, $\langle s_x \rangle$ ($\langle s_y \rangle = 0$) in their corresponding eigenstates as functions of the magnetic period λ , here in the units of the CNT unit cell length ($T_{\text{CNT}} = 1.127$ nm). The results were obtained with exact diagonalization method. The numbers in the plot denote the longitudinal modes, and the subscript a/p whether the configuration of valley and spin in the doublet is antiparallel or parallel, respectively. (b) Transmission through the same CNT, calculated with the Green's function method. Orange points mark the energy values from exact diagonalization shown in (a). The coupling to the leads is taken to be $\Gamma_L = \Gamma_R = 0.1$ meV.

$V_{pp}^\sigma = 6.38$ eV and $V_{pp}^\pi = -2.66$ eV are taken from Ref. [18], and the strength of the intrinsic spin-orbit coupling is determined by δ_{SO} , which is set to 10^{-3} in our calculation.

In presence of the magnetic field the hopping elements are modified by the Peierls phase Φ_{ij} . The gauge we chose for the cycloidal field is

$$\mathbf{A}_{\text{osc}} : A_{\text{osc},x} = A_{\text{osc},z} = 0, \quad A_{\text{osc},y} = \left(x - \frac{\lambda}{2\pi}\right) \sin\left(\frac{2\pi z}{\lambda} + \delta\right),$$

$$\mathbf{B}_{\text{osc}} : B_{\text{osc},x} = B_{\text{osc}} \left(1 - \frac{2\pi x}{\lambda}\right) \sin\left(\frac{2\pi z}{\lambda} + \delta\right), \quad B_{\text{osc},y} = 0, \quad B_{\text{osc},z} = B_{\text{osc}} \sin\left(\frac{2\pi z}{\lambda} + \delta\right).$$

Since $x \ll \lambda$, $B_{\text{osc},x} \approx B_{\text{osc}} \sin(2\pi z/\lambda + \delta)$, in agreement with the sinusoidal form of \mathbf{B} in Eqs. (6) and (7). We have included here also an arbitrary phase shift δ to account for shifting magnetization profiles. The main contribution to the orbital effect comes from $B_{\text{osc},z}$.

The external magnetic field is applied in the z direction, parallel to the CNT axis, with

$$\mathbf{A}_{\text{ext}} = (0, x B_{\text{ext}}, 0), \quad \mathbf{B}_{\text{ext}} = (0, 0, B_{\text{ext}}).$$

The code setting up the atomic lattice and the Hamiltonian is written in C++, using the Armadillo linear algebra library [19]. In the first step the Hamiltonian (12) is diagonalized directly, using sparse matrix algorithms from MATLAB. The energy levels for the first 32 states in the conduction band of a $(6,3)$ CNT with 400 unit cells [denoted as $(6, 3) \times 400$, with

$d = 0.62$ nm, $L = 450$ nm] in a $B_{\text{osc}} = 10$ T with varying λ and $\delta = 0$ are shown in Fig. 5(a). The spectrum splits into a series of doublets $n_{a/p}$, where n denotes the longitudinal mode, p the parallel ($\tau s = 1$) and a the antiparallel ($\tau s = -1$) alignment of the valley pseudospin and the electronic spin. The cycloidal field has two effects. First, it affects the position of the energy levels within each doublet, with the degeneracy restored whenever L is an integer multiple of λ , when the effects from the positive and negative $B_{\text{osc},z}$, $B_{\text{osc},x}$ components cancel out on average. The second effect is the mixing of longitudinal modes, which is stronger but limited only to the states for which the criterion of $\kappa_n \pm \kappa'_n = 2\pi/L$ is fulfilled. As far as the spin is concerned, in the cycloidal field the energy states are mostly eigenstates of s_z , except when the intermode mixing occurs and a discernible s_x component appears.

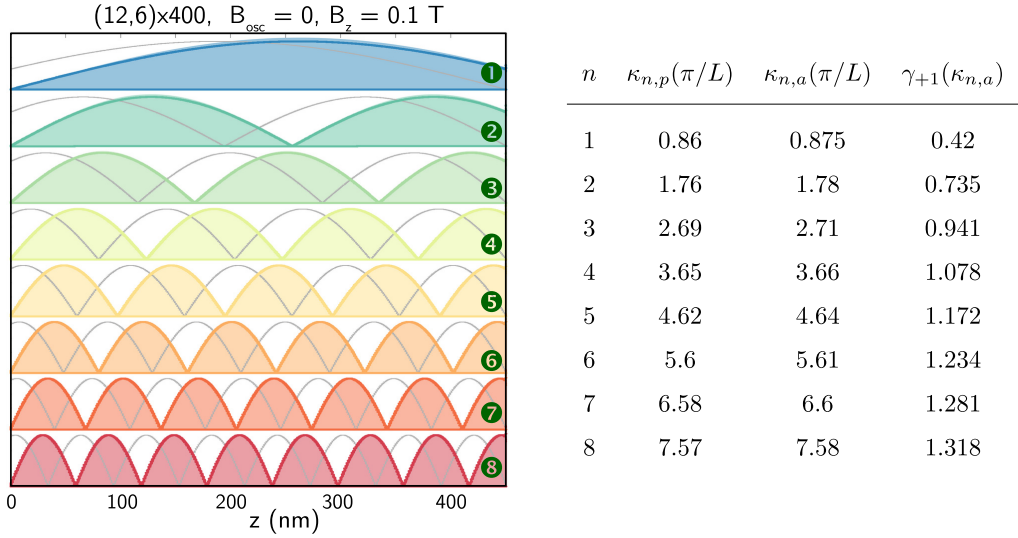


FIG. 6. The longitudinal profile of the modulus $|\psi_{n+}(K)|$ for the first eight eigenstates in the conduction band of a $(12, 6) \times 400$ CNT. The grey points mark the numerical data for sublattice B , the colored points the data for sublattice A . The colored background displays $|\sin(\kappa_n x)|$ with the values of κ_n in π/L units taken from the table on the right. As n increases, $\kappa_{n,a}$ of the antiparallel and $\kappa_{n,p}$ of the antiparallel Kramers doublets both converge to $(n - 1/2)\pi/L$. For this CNT, $\Delta k_{\perp} = -1.36 \times 10^{-3} \text{ \AA}^{-1}$, which corresponds to $\Delta k_{\perp} = -1.96\pi/L$.

The exact diagonalization is expensive in terms of computational time and resources. If we are interested mostly in the evolution of the energy levels and not in the eigenstates, we can turn to Green's function methods and associated decimation techniques [20]. In this approach the nanotube is connected to the wide-band leads ($\Gamma_L = \Gamma_R = 0.1 \text{ meV}$) and its transmission is calculated with the Meir-Wingreen-Lee formula [21]. The peaks of transmission occur at the poles of the Green's function, i.e., at energies matching those in the spectrum of the nanotube, as shown in Fig. 5(b). This is therefore our method of choice for the numerical calculation

of the larger $(12, 6) \times 400$ CNT with $d = 1.4 \text{ nm}$, closer to the experimental size.

The influence of B_{osc} on electronic eigenstates can be better understood in terms of the minimal model presented below. For the analytical calculation of the coefficients $\alpha_{nm}^{\sigma_x}$, $\alpha_{nm}^{\sigma_z}$, and β_{nm}^{τ} , we need to first identify the unperturbed quantum states.

D. Quantization of longitudinal modes

The eigenstates of the unperturbed CNT at low energies can be calculated from the Dirac Hamiltonian in the two valleys [15–17],

$$H_{\tau}(\kappa) = \hbar v_F \begin{pmatrix} 0 & e^{i\tau(\theta+\pi/3)}(\tau \Delta k_{\perp} + i\kappa) \\ e^{-i\tau(\theta+\pi/3)}(\tau \Delta k_{\perp} - i\kappa) & 0 \end{pmatrix}, \quad (15)$$

where θ is the chiral angle of the CNT. The momentum is calculated from the center of each valley, i.e., $\kappa = k - \tau K$, where K is the longitudinal momentum corresponding to the K point. In metallic nanotubes the transverse momentum of the Dirac subbands is τK_{\perp} , so $\kappa_{\perp} = 0$, but the curvature of the lattice results in an additional term opening a small band gap, $\Delta k_{\perp} = a_c(1 + 3(V_{pp}^{\sigma} - V_{pp}^{\pi})/(8V_{pp}^{\pi})) \cos 3\theta/(4R^2)$. The intrinsic spin-orbit coupling adds another, spin-dependent shift, $s\Delta k_{\text{SO}} \ll \Delta k_{\perp}$, cf. the table in Fig. 6. In the calculation of the matrix elements we will neglect Δk_{SO} . We can introduce an auxiliary phase

$$\gamma_{\tau}(\kappa) := \arg(\tau \Delta k_{\perp} + i\kappa) \quad \text{with} \quad \gamma_{\tau}(-\kappa) = -\gamma_{\tau}(\kappa), \quad (16)$$

so that the spinorial part of the Bloch states is

$$|u_{+}(\tau, \kappa)\rangle = \frac{1}{\sqrt{2}} \begin{pmatrix} 1 \\ e^{-i\tau(\theta+\pi/3)} \exp(-i\gamma_{\tau}(\kappa)) \end{pmatrix}, \quad |u_{-}(\tau, \kappa)\rangle = \frac{1}{\sqrt{2}} \begin{pmatrix} 1 \\ -e^{-i\tau(\theta+\pi/3)} \exp(-i\gamma_{\tau}(\kappa)) \end{pmatrix}, \quad (17)$$

for the conduction (+) and valence (−) bands, respectively. In a finite system, the eigenstates can be expressed as linear superpositions of Bloch states with opposite momenta,

$$|n_{\pm}(\tau)\rangle = \frac{1}{\sqrt{2}} (|\tau K_{\perp}, \tau K + \kappa_n\rangle \otimes |u_{\pm}(\tau, \kappa_n)\rangle - |\tau K_{\perp}, \tau K - \kappa_n\rangle \otimes |u_{\pm}(\tau, -\kappa_n)\rangle), \quad (18)$$

where κ_n is quantized [22] according to

$$\tau \Delta k_{\perp} = \kappa_n \tan \kappa_n L. \quad (19)$$

The quantization of κ_n depends then on the curvature-induced gap; when $\Delta k_{\perp} = 0$, this results in a half-integer quantization $\kappa_n = (n + 1/2)\pi/L$. When $\Delta k_{\perp} \gg 1/L$, the quantization approaches the standard quantum box condition, $\kappa_n = n\pi/L$.

For our $(12, 6) \times 400$ CNT, the first eight eigenstates in the conduction band and their corresponding momenta κ_n are shown in Fig. 6.

Another form of the quantization condition (cf. Eq. (9) in Ref. [23]) is

$$\sin\left(\kappa L - \frac{\gamma_\tau(\kappa) - \gamma_\tau(-\kappa)}{2}\right) = 0. \quad (20)$$

Together with (16), it tells us that

$$\kappa L - \gamma_\tau(\kappa) = \pi n, \quad m \in \mathbb{Z}. \quad (21)$$

It is not obvious, but n is indeed the quantum number of the longitudinal mode, counting the first nontopological state as $n = 1$. This will allow us to replace γ_τ in the following.

E. Matrix elements of H_{osc}

The matrix elements of H_{osc} between the unperturbed eigenstates (18) are introduced in Eqs. (6) and (7). Using the shorthand notation $\Delta\kappa := (\kappa_n - \kappa_{n'})/2$, $\bar{\kappa} := (\kappa_n + \kappa_{n'})/2$, $n_B := \pi L/\lambda$ and $\Delta n := n - n'$, we find the analytical expressions for the coefficients $\alpha_{nn'}^{\sigma_x}$, $\alpha_{nn'}^{\sigma_z}$, and $\beta_{nn'}^{\tau_z}$,

$$\alpha_{nn'}^{\sigma_x} = \frac{1}{4}\{\mathcal{S}_-(n, n', \lambda)[\cos(\Delta\kappa L + n_B + \delta) + (-1)^{\Delta n} \cos(\Delta\kappa L - n_B - \delta)] - \mathcal{S}_+(n, n', \lambda)[\cos(\bar{\kappa}L + n_B + \delta) + (-1)^{\Delta n} \cos(\bar{\kappa}L - n_B - \delta)]\}, \quad (22)$$

$$\alpha_{nn'}^{\sigma_z} = \frac{1}{4}\{\mathcal{S}_-(n, n', \lambda)[\sin(\Delta\kappa L + n_B + \delta) - (-1)^{\Delta n} \sin(\Delta\kappa L - n_B - \delta)] - \mathcal{S}_+(n, n', \lambda)[\sin(\bar{\kappa}L + n_B + \delta) - (-1)^{\Delta n} \sin(\bar{\kappa}L - n_B - \delta)]\}, \quad (23)$$

where

$$\mathcal{S}_\pm(n, n', \lambda) := \frac{\sin((\kappa_n \pm \kappa_{n'})L/2 + n_B)}{(\kappa_n \pm \kappa_{n'})L/2 + n_B} + (-1)^{\Delta n} \frac{\sin((\kappa_n \pm \kappa_{n'})L/2 - n_B)}{(\kappa_n \pm \kappa_{n'})L/2 - n_B}.$$

In order to calculate $\beta_{nn'}^{\tau_z}$ analytically, we first notice that the local tangential component of \mathbf{A}_{osc} , $A_\varphi = B_{\text{osc}}R \sin(2\pi z/\lambda)/2$ is the main factor determining the Peierls phase. The phase acquired upon hopping between atoms j and i is then given by

$$\Phi_{ij} = \frac{\pi R^2}{\phi_0} B_{\text{osc}} \sin(2\pi \bar{z}/\lambda)(\varphi_i - \varphi_j),$$

where $\phi_0 = h/e$ is the magnetic flux quantum and $\bar{z} = (z_i + z_j)/2$. The expression for the dimensionless coefficient $\beta_{nn'}^{\tau_z}$ is then

$$\beta_{nn'}^{\tau_z} = \frac{(-1)^{n+1}}{4}\{\mathcal{S}_-(n, n', \lambda)[\sin(\bar{\kappa}L + n_B + \delta) - (-1)^{\Delta n} \sin(\bar{\kappa}L - n_B - \delta)] - \mathcal{S}_+(n, n', \lambda)[\sin(\Delta\kappa L + n_B + \delta) - (-1)^{\Delta n} \sin(\Delta\kappa L - n_B - \delta)]\}. \quad (24)$$

The value of g_{orb} is $ev_F R/2$. The evolution of the matrix elements, both calculated numerically and analytically, is shown in Fig. 7(b), for a CNT $(12,6) \times 400$ —twice wider than the $(6,3)$ shown in Fig. 5. While the $n' = n$ elements exhibit one resonance, at $\bar{\kappa} = \kappa_n = \pi/\lambda$, for the $n' \neq n$ another resonance appears at high λ , corresponding to $\Delta\kappa = \pi/\lambda$. The numerical and analytical matrix elements show excellent agreement, except for $\alpha_{n,n' \neq n}^{\sigma_z}$ at high λ . This discrepancy is not yet understood but does not change qualitatively our results.

The coefficients describing the effect of intermode coupling due to the texture are given by

$$\gamma_{nn}^{\sigma_0} = E_{\text{SO}} \sum_{l \neq n} \frac{|\alpha_{ln}^{\sigma_z}|^2 + |\alpha_{nl}^{\sigma_x}|^2}{E_l - E_n}, \quad \gamma_{nn}^{\tau_0} = E_{\text{SO}} \sum_{l \neq n} \frac{|\beta_{nl}^{\tau_z}|^2}{E_l - E_n}, \quad \gamma_{nn}^{\sigma_z \tau_z} = E_{\text{SO}} \sum_{l \neq n} \frac{\beta_{nl}^{\tau_z} \alpha_{ln}^{\sigma_z} + \alpha_{nl}^{\sigma_z} \beta_{ln}^{\tau_z}}{E_l - E_n}, \quad (25)$$

$$\gamma_{nn}^{\sigma_x \tau_z} = E_{\text{SO}} \sum_{l \neq n} \frac{\beta_{nl}^{\tau_z} \alpha_{ln}^{\sigma_x} + \alpha_{nl}^{\sigma_x} \beta_{ln}^{\tau_z}}{E_l - E_n}, \quad \gamma_{nn}^{\sigma_y} = iE_{\text{SO}} \sum_{l \neq n} \frac{\alpha_{nl}^{\sigma_z} \alpha_{ln}^{\sigma_x} - \alpha_{nl}^{\sigma_x} \alpha_{ln}^{\sigma_z}}{E_l - E_n}, \quad (26)$$

where $E_{\text{SO}} = hv_F/\lambda$, as before. Both analytical models reproduce nicely the numerical results, as shown in Fig. 8, with the full model [Eqs. (6) and (7)] yielding a slightly better quantitative agreement with the numerics than the Schrieffer-Wolff transformed projection on a single mode [Eqs. (8) and (9)]. Eigenstate spins are oriented predominantly in the z direction, except when $\alpha_{nn'}^{\sigma_x}$ becomes significant. Interestingly, the synthetic spin-orbit depends strongly on the phase δ —even for $\lambda = 200T_{\text{CNT}} = L/2$, where both $B_{\text{osc},x}$ and $B_{\text{osc},z}$ components average out to 0, the levels which are degenerate at $\delta = 0$ become strongly split when

$\delta = 90^\circ$. This confirms again that the interplay between the nanotube's wave functions and the profile of the texture is a crucial factor determining the synthetic spin-orbit coupling.

F. Magnetic texture and external magnetic field

In order to model the dependence of the synthetic spin-orbit coupling on the external magnetic field, we take as our starting point the results of the micromagnetic simulations discussed in E and adjust their output parameters, guided by the experimental data.

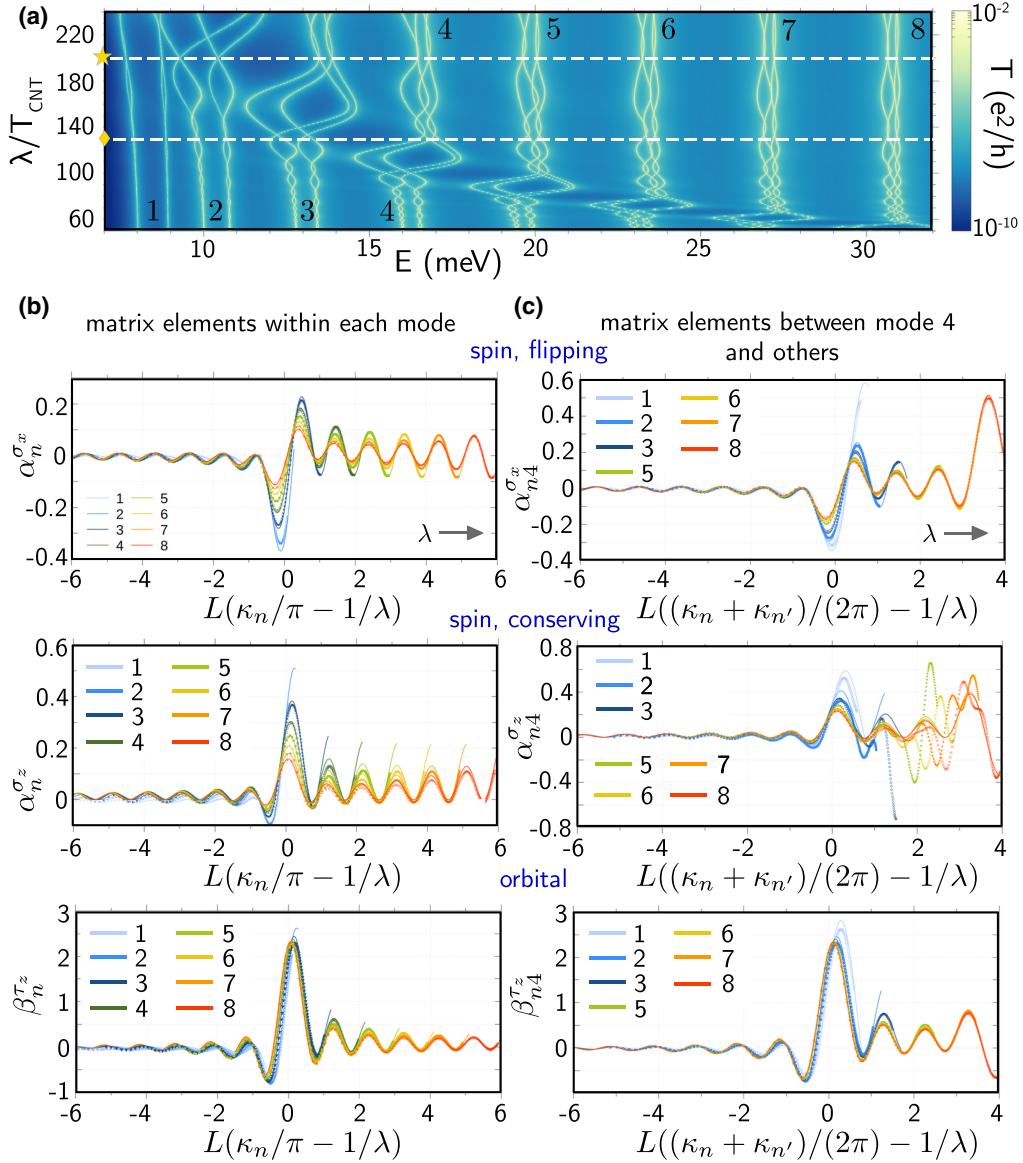


FIG. 7. Perturbation caused by the cycloidal magnetic field. (a) Transmission through a $(12, 6) \times 400$ CNT ($d = 1.25$ nm, $L = 451$ nm), with $B_{\text{osc}} = 10$ T, $\delta = 0$, and $\Gamma_L = \Gamma_R = 0.1$ meV, displaying the longitudinal mode numbers for each valley/spin quadruplet. Dashed white lines mark the values of λ_0 for which the results shown in Fig. 9 were obtained. The cycloidal field does not couple different valleys, but it can mix both spins and the longitudinal modes [cf. Eq. (6) and (7)]. The matrix elements within each longitudinal mode $\alpha_n^{\sigma_x}$, $\alpha_n^{\sigma_z}$, and $\beta_n^{\tau_z}$ are shown in column (b), the matrix elements between mode $n' = 4$ (chosen for illustration) and modes $n \neq 4$ are shown in column (c). The horizontal axis is $[(\kappa_n + \kappa_{n'})/2 + \pi/\lambda]L/\pi$, showcasing the common resonance (or antiresonance in case of α^{σ_x}) at 0.

Based on the results shown in Fig. 15, we model the variation of B_{osc} as

$$\lambda(B_{\text{ext}}) = \lambda(0) + \frac{d\lambda}{dB_{\text{ext}}} B_{\text{ext}},$$

$$B_{\text{osc}}(B_{\text{ext}}) = B_{\text{osc}}(0) + \frac{dB_{\text{osc}}}{dB_{\text{ext}}} B_{\text{ext}}. \quad (27)$$

The parameters in the simulations take the values $\lambda(0) = 112$ nm, $B_{\text{osc}}(0) = 0.234$ T, $d\lambda/dB_{\text{ext}} = -93$ nm/T, and $dB_{\text{osc}}/dB_{\text{ext}} = -185$ mT/T.

The first adjustment is based on the MFM data, shown in Fig. 1(c) with $\lambda \simeq 160$ nm, thus we modify $\lambda(0)$ upwards.

Since the experimental results display few kinks, $\lambda(0)$ is likely close to an integer fraction of L , where $E_n(\lambda)$ do not feature many crossings (cf. Fig. 8). We choose three initial values of $\lambda(0)$, namely $L/3 = 149.9$ nm, $L/2 = 225.4$ nm, and $L/2.2 = 202.9$ nm.

The second adjustment is motivated by the giant g_{orb} values recorded in the experiment. They indicate a much stronger influence of the magnetic texture than the value of $B_{\text{osc}}(0) = 0.234$ T would imply. The texture may be interacting with the nanotube not only through the stray field, but also by direct exchange interaction mediated by impurities [24] in the aluminium oxide thin layer separating the texture and the nanotube. Since we cannot reliably estimate the correct

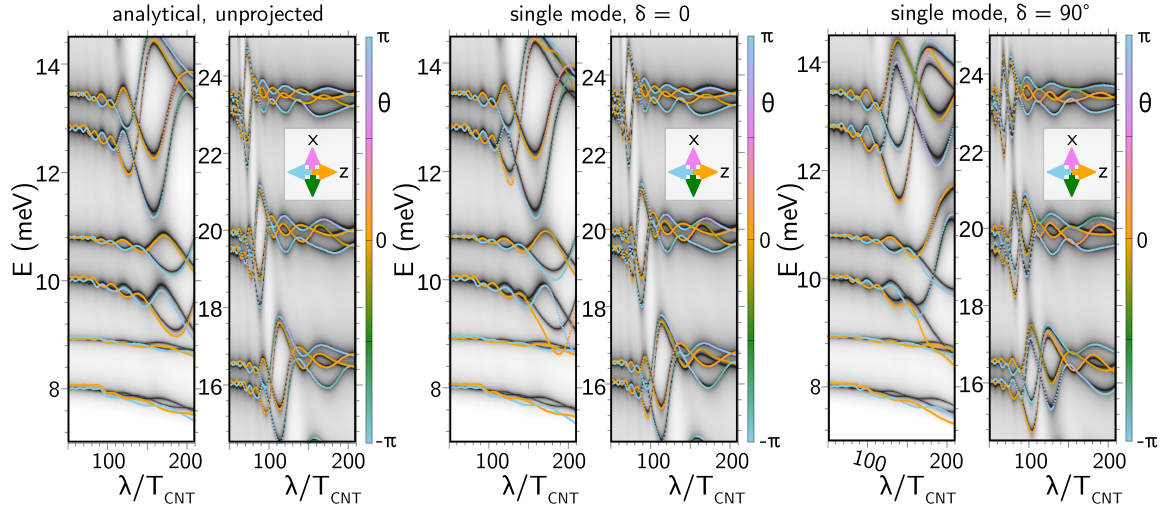


FIG. 8. Numerical vs analytical results. Comparison of the numerical results from a transmission calculation (greyscale background, dark corresponds to transmission peaks) and the analytical model (colored points), either diagonalizing the full analytical Hamiltonian [Eqs. (6) and (7)] with the first 32 states (leftmost two panels) or the Schrieffer-Wolff transformed Hamiltonian [Eq. (8)] projected onto each mode (remaining panels). Color denotes the orientation of the eigenstate’s spin in the xz plane, $\theta_{xz} = \arctan(\langle s_x \rangle / \langle s_z \rangle)$.

B_{osc} , we keep our initial value of $B_{\text{osc}}(0) = 10$ T and rescale $dB_{\text{osc}}/dB_{\text{ext}}$ by a factor of $10/0.243$ —this rescaling is the most arbitrary step in our simulation. As shown in the main text and in Fig. 9, the resulting evolution of energy levels in B_{ext} displays low field slopes consistent with the giant g_{eff} factors observed in the experiment. In order to correctly model the effect of the texture we would need both a better understanding of the exchange interaction between the texture and the nanotube, and the knowledge of the nanotube’s diameter and chirality.

All the above discussion allows us to fully justify both the low-energy Hamiltonian derived from the Schrieffer-Wolff transformation as well as the basic dependence of the

parameters entering in it as a function of the control parameters of the systems like the characteristic oscillation period of the texture as well as the external magnetic field. As shown in Fig. 4(d), we are able to reproduce the observed findings using the assumption that the magnetic field dependence is symmetric. The energy levels correspond to an electron filling $n_1=11$ for the left dot and $n_2=23$ for the right dot.

The assumption of symmetric dependence of the magnetic properties entering in the model Hamiltonian, while not fully obvious in the free energy of the magnetic system, is natural if one assumes that the magnetic system is always in its ground state, which should be symmetric with respect to positive and

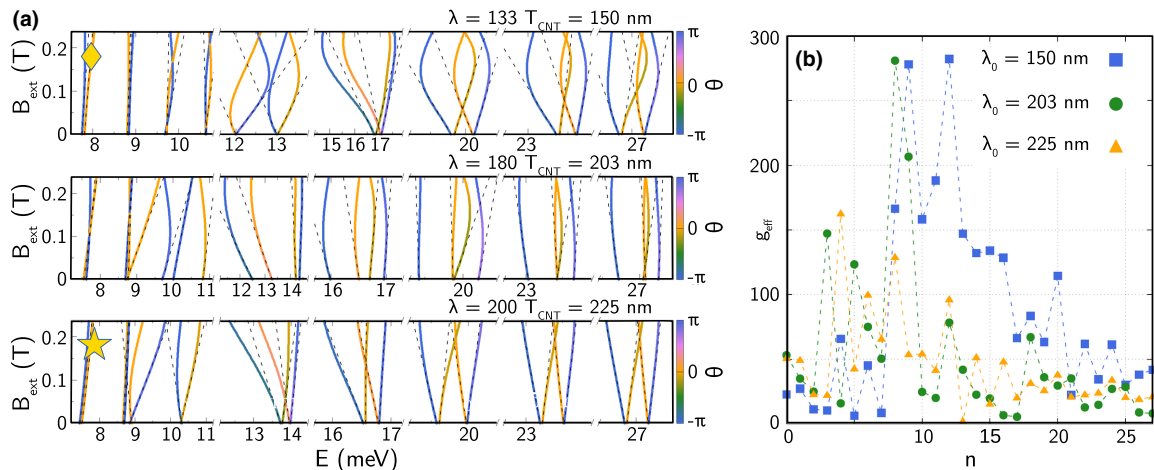


FIG. 9. Evolution of the CNT energy levels in external magnetic field B_{ext} . (a) Energy levels of a $(12, 6) \times 400$ CNT ($d = 1.25$ nm, $L = 451$ nm) nanotube, with initial $B_{\text{osc}} = 10$ T, $\delta = 0$ and initial λ_0 indicated in the plot. The variation of B_{osc} and λ with B_{ext} is given in the text. From the low-field linear fits shown with dashed black lines, the effective g_{eff} values shown in (b) are extracted, through $g_{\text{eff}} = \Delta E / (\mu_B \Delta B_{\text{ext}} / 2)$.

negative magnetic field. This is therefore not a very strong assumption. The most surprising result of our study is the 10 T of field amplitude needed to explain the observed effects. Exchange effects are expected to have the same qualitative behavior as stray fields since they also follow the magnetization profile but are expected to be much larger as far as magnitude and inhomogeneity are concerned. The real space modeling performed above shows that we are not missing anything in the low-energy effective theory. As a consequence, the outcome of our study is that magnetic fields with the same spatial dependence as that we have characterized but much larger amplitude than possible through stray field effect are needed to explain our data. The only mechanism possible for that is through an exchange interaction which will have to be studied in future works. We admit that this is a hypothesis at this stage which is substantiated by the large values of the effective Landé factors. This is why we think that the simple model is important. Overall, the simple double quantum dot model with inhomogeneous very large Landé factors is the simplest explanation which stems from the giant dispersion of the spinful states as a function of the magnetic field. In order to further substantiate this, low temperature measurements of the evolution of the magnetic texture in particular would be very insightful.

V. QUANTITATIVE MODELLING OF THE MAGNETO-SPECTROSCOPY

We study now in detail the evolution of the phase contrast dispersion for different dot orbital states, labeled with indices i_L and i_R , obtained for different $V_{gR}-V_{gL}$ gate configurations. Figure 10(a) displays the corresponding measurements of the phase contrast as a function of $B_{\text{ext}}-E_d$ for several bonding-antibonding transitions in the staggered sample, subsequently named interdot transitions. As expected for an orbitally sensitive phenomenon and illustrated in Figs. 3(b) and 3(c), there are strong qualitative variations for the phase contrast dispersion depending on the considered orbital states. The observed dispersions range from a “v-shape” going up or down to a “w-shape” going up or down, the reversed “w-shape” of Fig. 2(d) being one particular example. In addition, there are changes in the magnitude and sign of the phase contrasts as a function of the external magnetic field. As a consequence, these measurements show that there are spinful levels whose dispersions change as the orbital part of the wave function is changed, as expected for spin-orbit interaction. Since, like in Fig. 2(d), the dispersion is greater than the width of the phase contrasts stripe, we are led to conclude that the spin-orbit interaction engineered in our setup is in the strongly inhomogeneous regime, i.e., has a staggered character between the two dots. This means that our setup can be a building block for longer chains which could host topological excitations. This is the main result of our work.

We now show that we can explain quantitatively our findings for the existence of a staggered spin-orbit interaction. The numerical calculations of the nanotube spectrum in a cycloidal field confirm our analytically obtained low-energy Hamiltonian. It is enough to consider the ground and first excited state of such a Hamiltonian here since we are interested in the quasi resonant response of the DQD to the

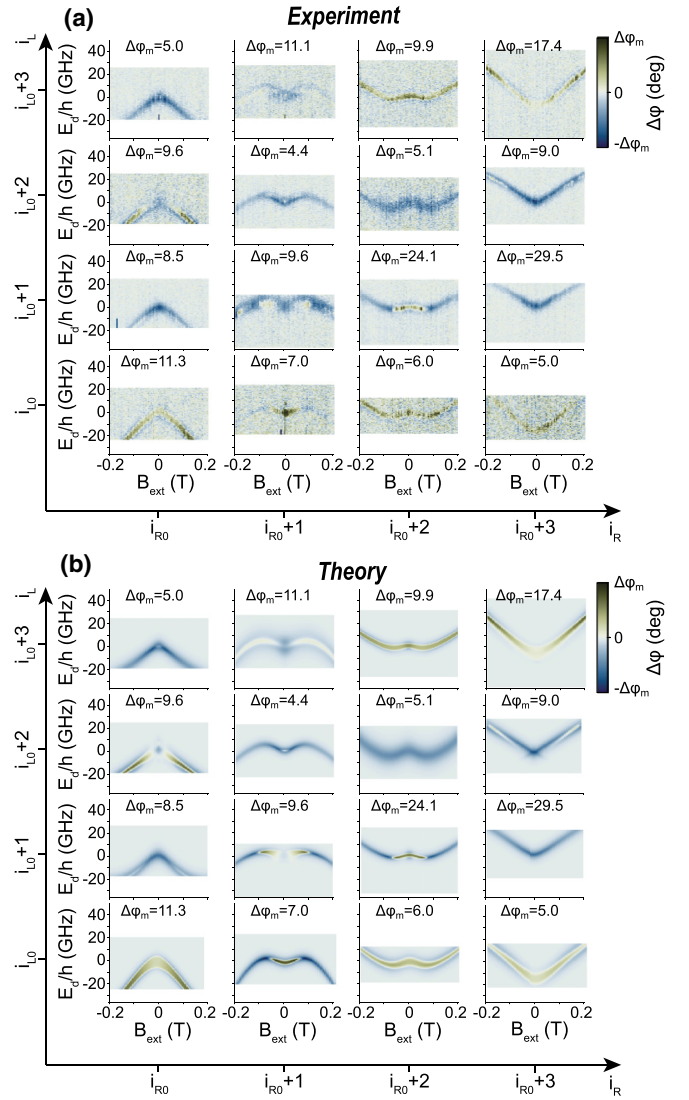


FIG. 10. Orbital effect on spinful transitions. (a) Measured $B_{\text{ext}}-E_d$ phase shift maps for several interdot transitions in the main sample, labeled by indexes i_L and i_R from an arbitrary origin i_{L0}, i_{R0} . The colorbar scale is symmetric and its maximum value is given by $\Delta\phi_m$ displayed for each interdot transition (i_L, i_R). (b) Simulations of the cavity phase shift signal for the interdot transitions of (a) using the local fields and effective g model.

cavity photons. This leads us to consider our device using a two level system Hamiltonian which can be mapped onto an effective spin qubit model [8,25]. The left and right dots are subject to a local effective field $B_{L(R)}$ with a relative angle θ in the $x-y$ plane and have effective Landé factors $g_{L(R)}$. As shown in Figs. 3(b) and 3(c), these effective parameters stem from the interplay of the local magnetic field modulations and the electronic wave function and, while they are related to the magnetic texture, do not map directly onto the real magnetic field “felt” by the electrons. We therefore consider them as fitting parameters. The external magnetic field B_{ext} is applied along the CNT axis z and B_L is taken along the x axis. All the ingredients of such a low-energy model can be obtained by considering the effect of the magnetic texture on a carbon nanotube. In particular, the perturbed spinful energy

levels acquire a magnetic field dependent orbital part which strongly renormalizes the effective Landé factors. Since the magnetic field dispersion of the spinful levels in each dot is related to the overlap between the electronic wave function and magnetic texture stray field, there are two ways to control it, either by detuning each dot or by changing the value of the external magnetic field, as illustrated in Figs. 3(b) and 3(c). As shown in Fig. 10(b), we can quantitatively reproduce the variety of experimental observations. The obtained orders of magnitude of $B_{L(R)}$, θ and $g_{L(R)}$ are 100–500 mT, 0– 0.95π , 1–200, and $t \approx 3$ –7 GHz. Besides the qualitative dependence on the orbital and inhomogeneity, it is worth noticing that the extracted values of Landé factors are much larger than the observed values in the literature [22,26,27] and in our control devices. This allows us to rule out a simple orbital effect for our measurements. All these facts confirm that we have achieved the strong inhomogeneity regime of spin-orbit interaction.

As a conclusion, we have demonstrated using high resolution microwave spectroscopy that magnetic textures can be used to engineer strong changes in the magnitude and direction of a synthetic spin-orbit interaction. As such, our device is an elementary two site chain which can display a staggered spin-orbit interaction. Importantly, our approach is scalable in the sense that many such sites can be built lithographically and compatible with a single single wall carbon nanotube using our nanoassembly technique. Since nanotubes CVD grown easily span 30 μm , we can envision 10–20 site chains to be built experimentally. Such a synthetic material could have important applications for the engineering of topologically nontrivial states either Majorana mode related if combined with superconductors using the central electrode as both a gate and a contact or more generally charge and spin magnetically textured states.

$$T = \frac{\kappa/2}{-i\kappa/2 - \frac{g_0^2}{8t\sqrt{1+(\frac{E_d}{2t})^2}} \frac{1}{\sqrt{1+(\frac{E_d}{2t})^2} - \frac{f_{\text{cav}}}{2t} - i\frac{\Gamma_2}{4t}} \tanh\left(\frac{t}{k_B T_e} \sqrt{1 + \left(\frac{E_d}{2t}\right)^2}\right)}, \quad (\text{B1})$$

as a function of $E_d/2t$, with $\Gamma_2 = \Gamma_1 + \Gamma_\phi/2$. Typical energy scales for our experiments are $g_0 \sim 20$ MHz, $\Gamma_2 \sim 1$ GHz for the charge, $f_{\text{cav}} \sim 6$ GHz $\equiv 0.3$ K and $T_e = 0.8 - 0.15$ K. We consider three different regimes of t for characterizing the width of the cavity phase signal which is approximately equal to $\Delta\phi = \frac{2}{\kappa} \Re[\chi](n_+ - n_-)$.

(1) $t \gg hf_{\text{cav}}/2$ implying $t \gg \Gamma_2/4$ and $t \gg k_B T_e$. In this regime, $\tanh \approx 1$ and $\Delta\phi$ reduces to

$$\Delta\phi \approx \frac{2}{\kappa} \frac{g_0^2}{8t} \frac{1}{\left[1 + \left(\frac{E_d}{2t}\right)^2\right]^{3/2}}, \quad (\text{B2})$$

which varies on an energy scale $2t$ and has a width at half maximum of about $3t$ and whose amplitude decreases as $1/t$.

ACKNOWLEDGMENTS

We would like to thank Milena Grifoni, Jelena Klinovaja, and Daniel Loss for fruitful discussions. The work has been supported by the QuantERA project SuperTop and by the ANR project MITIQ.

APPENDIX A: FITTING DETAILS

The electronic temperature is taken to be $T_e = 150$ mK. $g_{\text{orb}} = 10$, $\Delta_{KK'} = 6$ GHz, and $\kappa = 5.5$ MHz. $\Gamma_{\phi,v} = \Gamma_{\phi,s} = 1$ MHz by default. As g_{orb} is taken identical on the left and right dot (we assume that the filling is not very different in the two dots [14,26]), it has no effect on the dispersion which is only sensitive in gradients. The cavity resonance frequency f_{cav} and the drive frequency f_d are magnetic field dependent with values ranging from 6.415 to 6.43 GHz. Exact values of $f_{\text{cav}}(B_{\text{ext}}) = f_d(B_{\text{ext}})$ are taken from characterization of the cavity resonance shift with B_{ext} , as shown below.

APPENDIX B: WIDTH OF AN INTERDOT TRANSITION CAVITY SIGNAL

In order to understand the shape of the phase (and amplitude) signal of the transmitted cavity field [Eq. (1)], we will consider the case of a single transition from the model above, for the sake of simplicity. We thus have $f_{ij} = f_q = \sqrt{E_d^2 + 4t^2}$, $g_{ij} = \tilde{g} = \frac{g_0 t}{\sqrt{E_d^2 + 4t^2}}$, and $n_i - n_j = n_+ - n_- = \frac{1}{Z}(e^{E_+/k_B T_e} - e^{E_-/k_B T_e})$ with $E_\pm = \pm \frac{1}{2}\sqrt{E_d^2 + 4t^2}$, $Z = e^{E_+/k_B T_e} + e^{E_-/k_B T_e}$ and k_B the Boltzmann constant. It yields $n_+ - n_- = \tanh\left(\frac{\sqrt{E_d^2 + 4t^2}}{2k_B T_e}\right)$. Note that populations are estimated with Boltzmann factors as we restrict to the single particle situation which is equivalent to considering the noninteracting case. In addition, the cavity readout drive is set to $f_d = f_{\text{cav}}$ giving

(2) $t > hf_{\text{cav}}/2$ implying $t \gg \Gamma_2/4$ and $t \gg k_B T_e$. In this regime, $\tanh \approx 1$ and $\Delta\phi$ reduces to

$$\Delta\phi \approx \frac{2}{\kappa} \frac{g_0^2}{8t} \frac{1}{\left[1 + \left(\frac{E_d}{2t}\right)^2\right]^{3/2}} \frac{1}{1 - \frac{f_{\text{cav}}}{\sqrt{E_d^2 + 4t^2}}}, \quad (\text{B3})$$

still varying on an energy scale $2t$ and whose width at half maximum is larger than in the previous regime, thus larger than $3t$.

(3) $k_B T_e < t < hf_{\text{cav}}/2$. In this regime, Eq. (B1) cannot be simplified. The two energy scales on which $\Delta\phi$ varies are $2t$ (as in previous regimes) and $\sqrt{f_{\text{cav}}^2 - 4t^2}$, which sets when the function changes signs at the resonance between the transition and the cavity resonance frequency. As t decreases from $f_{\text{cav}}/2$, the width of the phase signal increases from $\gtrsim 3t$ to $\approx 2\sqrt{f_{\text{cav}}^2 - 4t^2}$.

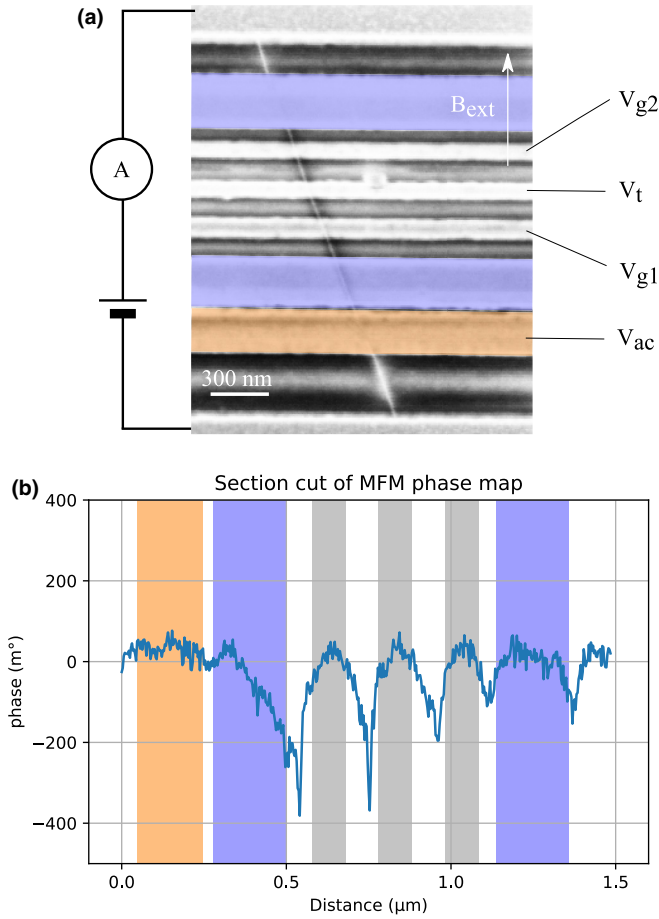


FIG. 11. Magnetic characterization on control device. (a) False-color SEM image of the control device, with the CNT appearing in white. The external orange gate is connected to the cavity central conductor. The two lateral blue gates are made of CoPt. (c) MFM phase cut of the sample, acquired in lift mode, displaying no modulations above the magnetic gates (blue region). We attribute this both to the single domain structure of the stripes “seen” by the nanotube and to the weaker magnetic stray field produced by the layer as compared to the one of the staggered device. The large dips in the MFM signal are due to spurious topographic effects.

(4) $t \ll k_B T_e < hf_{\text{cav}}/2$. In this regime, $\tanh \rightarrow 0$ as the two states become equally thermally populated and the cavity phase signal drops to zero. Interdot transitions with $t \lesssim k_B T_e$ are thus hardly measurable. Typically $hf_{\text{cav}} \approx 2 - 5k_B T_e$ in our experiments thus in the resonant regime ($t < hf_{\text{cav}}/2$) only interdot transitions with $t \sim hf_{\text{cav}}$ are observed.

APPENDIX C: CONTROL SAMPLE CHARACTERIZATION

We have reproduced the magnetic characterization of the magnetic electrodes in the case of the control sample, using equivalent scan settings for magnetic force microscope (MFM) and a similar magnetic tip. An SEM observation of the gates geometry [Fig. 11(a)] is added to the MFM data in Fig. 11(b). Only a small variation of the phase contrast occurs between the gates due to topographic cross-talk, which

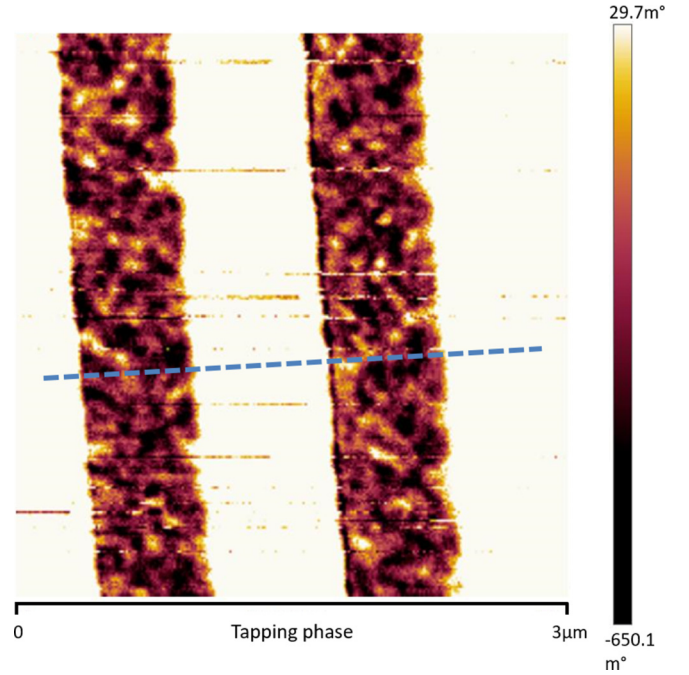


FIG. 12. 2D MFM image of the magnetic gates of the main device. MFM measurements of the gates of the main device showing the domain pattern of the CoPt stack. The domain structure is disordered but a 1D cut displays quasiperiodic contrast since the domain size distribution is peaked around ≈ 100 nm.

indicates a negligible contribution of the magnetic stray fields from the gates at the dot locations.

APPENDIX D: TRANSPORT VERSUS CAVITY MEASUREMENTS

It is important in this note to make a difference between our cavity measurements and the usual transport measurement made by the community. As explained in the main text, our measurements focus on the interdot transitions which do not change the total number of charge carriers on the nanotube device. Our measurements are sensitive to internal transitions between the ground state and the first excited state of the DQD spectrum. This contrasts with the transport measurements which are directly sensitive to changes in the ground state corresponding to particle nonconserving processes. In addition, although transport experiments are *a priori* sensitive to internal transitions indirectly also, they do not allow one to directly probe the hopping between the two dots with a conventional low-frequency setup.

APPENDIX E: MICROMAGNETIC SIMULATIONS OF CO/PT MULTILAYER GATES

In this Appendix, we describe the results of micromagnetic simulations, modeling the cycloidal magnetic texture adopted in the Co/Pt multilayer gates of sample 2, and the magnetic stray field patterns that they produce. The simulations have been performed for different values of the external magnetic field $B_{\text{ext}} = \mu_0 H_{\text{ext}}$, in order to obtain the external field depen-

dence of the details of the magnetic texture. The experimental MFM 2D map of our magnetic textures is represented in Fig. 12.

$$\frac{1}{N\lambda} \sum_{i=1}^N \int_0^\lambda dx A [\nabla \vec{m}^{(i)}]^2 + D [m_z^{(i)} \nabla \cdot \vec{m}^{(i)} - (\vec{m}^{(i)} \cdot \nabla) m_z^{(i)}] - K_u [m_z^{(i)}]^2 - \mu_0 M_s \vec{H}_{\text{ext}} \cdot \vec{m}^{(i)} \quad (\text{E1})$$

$$- \frac{\mu_0 M_s}{2} \vec{H}_{\text{dem}}^{(i)} \cdot \vec{m}^{(i)} - \frac{\mu_0 M_s H_{\text{iec}}}{2} [\vec{m}^{(i)} \cdot \vec{m}^{(i-1)} + \vec{m}^{(i)} \cdot \vec{m}^{(i+1)}], \quad (\text{E2})$$

whose magnetic interaction terms are defined below, which describes the micromagnetic energy density of an ensemble of N magnetic layers whose translationally invariant magnetic profiles $\vec{m}^{(i)}(x)$ have a defined periodicity λ along the direction transverse to the domains (designated x). The thin magnetic layers have a uniform magnetization across their thickness, but the $\vec{m}^{(i)}(x)$ can be different in the N layers. Here, \vec{m} refers to the reduced magnetization vector, being the volume magnetization \vec{M} normalized by the saturation magnetization M_s . The second line of Eq. (E1) accounts for the interaction between the magnetic layers. The demagnetiz-

ing field $\vec{H}_{\text{dem}}^{(i)}$ is computed in each layer i by solving the magnetostatic potential equations with the magnetic profiles $\vec{m}^{(i)}(x)$ in all layers as the source term. The interlayer exchange coupling term takes into account the direct electronic coupling between the magnetization in successive layers, here separated only by a thin Pt layer. The $\vec{m}^{(i)} \cdot \vec{m}^{(i-1)}$ and $\vec{m}^{(i)} \cdot \vec{m}^{(i+1)}$ terms are not present for layer $i = 1$ and $i = N$, respectively.

We proceed with the simulation of a magnetic system of size λ that contains two magnetic domains up ($m_z > 0$) and down ($m_z < 0$), respectively, and implement periodic boundary conditions in x , thus modeling the continuous magnetic texture of the Co/Pt electrodes. The magnetization in the domain boundaries is initialized in-between Néel and Bloch configurations, thus with $|m_x(x)| = |m_y(x)|$. The period λ is discretized into 128 cells, and we consider $N = 10$ layers. By varying λ at a given B_{ext} along y , we are able to find the domain period λ minimizing the overall magnetic energy and therefore get the field-dependent period $\lambda(B_{\text{ext}})$. The ten magnetic layers each have a thickness $t = 1.5$ nm, and are spaced vertically with a periodicity $p = 2.5$ nm. The values of the magnetic parameters for each Co layer inside the Co/Pt multilayer are symmetric exchange term $A = 10$ pJ/m; asymmetric exchange term $D = 0$ mJ/m² (Dzyaloshinskii-Moriya interaction terms are overall compensated due to the symmetric repetitions of Pt and Co); perpendicular magnetic anisotropy energy $K_u = 1.0$ MJ/m³ (which corresponds to an effective anisotropy $K_{\text{eff}} = 0.1$ MJ/m³ for a planar system); and saturation magnetization $M_s = 1.2$ MA/m for Co, as determined by SQUID magnetometry performed on patterned devices. In addition, the direct electronic coupling between the Co layers through Pt is taken into account by an interlayer exchange term $B_{\text{iec}} = 1.0$ T.

An example of minimized magnetic domains profile obtained for $\lambda = 100$ nm and $B_{\text{ext}} = 100$ mT is displayed in Fig. 13. The orientation of the magnetization inside the domain walls rotates across the different layers, from Néel ($|m_x(x)| > |m_y(x)|$) in the bottom layers to Bloch ($|m_x(x)| < |m_y(x)|$) configuration in the central layers, and to Néel again in the top layers, due to interlayer dipolar interactions.

The results of the energy minimization procedure are shown in Figs. 14(a) and 14(b). The red line in Fig. 14(a) indicates the domains period $\lambda(B_{\text{ext}})$ minimizing the micromagnetic energy density at each value of the external field. This line is reported in Fig. 14(b), which displays the amplitude of the cycloidal dipolar stray field $|B_{\text{osc}}|$ generated at a

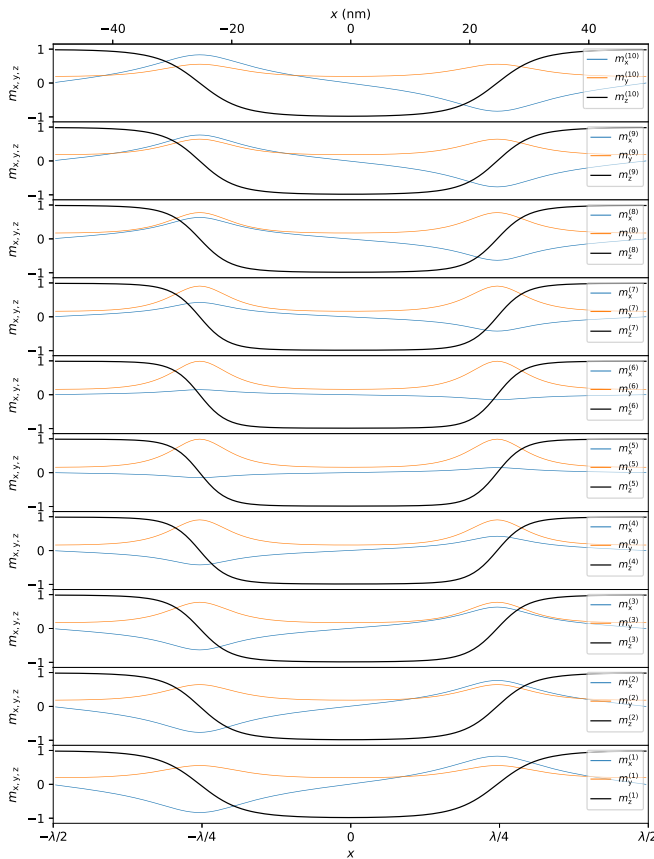


FIG. 13. Example magnetic profile obtained for $\lambda = 100$ nm and $B_{\text{ext}} = 100$ mT. Each panel displays the three component of the magnetization vector $m_x(x)$ (blue), $m_y(x)$ (orange), and $m_z(x)$ (black) in layer i .

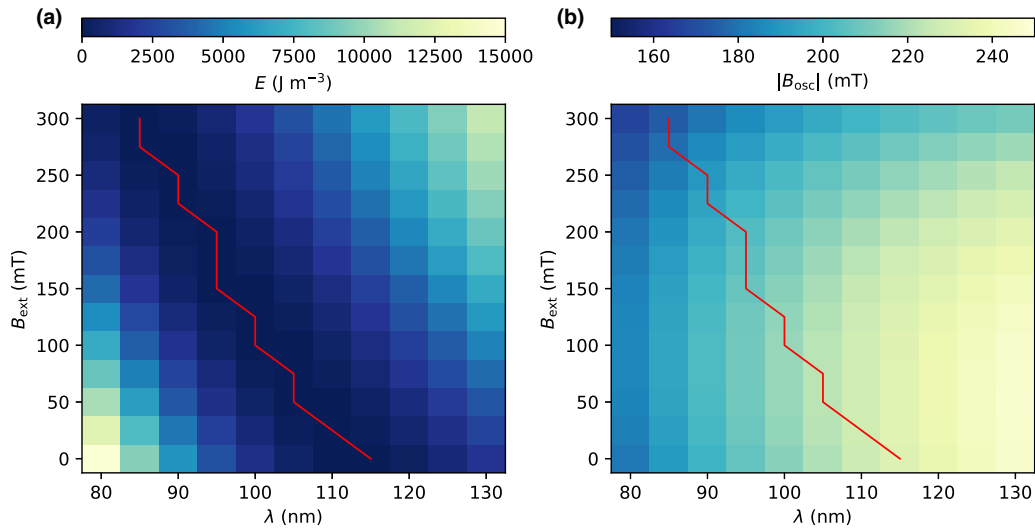


FIG. 14. Micromagnetic energy minimization results. (a) Micromagnetic energy density E in the magnetic layers as a function of domains period λ and external field B_{ext} . (b) Amplitude of the cycloidal stray field $|B_{\text{osc}}|$ at 10 nm above the magnetic layers as a function of domains period λ and external field B_{ext} . In each panel, a red line indicates $\lambda(B_{\text{ext}})$ minimizing the micromagnetic energy density.

height of 10 nm above the texture, considered the height of the CNT lying directly on the electrodes. Note that $\lambda(B_{\text{ext}})$ is also the period of the cycloidal stray field generated above the electrodes. The evolution of $\lambda(B_{\text{ext}})$ and $|B_{\text{osc}}|(B_{\text{ext}})$ is reported in Figs. 15(a) and 15(b), respectively. Linear fits to the discrete simulation data points provide figures for the external field susceptibility of the cycloidal dipolar stray field period and amplitude, providing $\lambda = 112 \text{ nm} - (93 \text{ nm/T}) B_{\text{ext}}(\text{T})$ and $|B_{\text{osc}}| = 234 \text{ mT} - (185 \text{ mT/T}) B_{\text{ext}}(\text{T})$. These relations are used for the numerical computation of the CNT spectra as a function of the external field.

The cycloidal dipolar stray field B_{osc} is analyzed in more details in Fig. 16. The spatial evolution of the horizontal $B_{\text{osc},x}$ and vertical $B_{\text{osc},z}$ components of the cycloidal dipolar stray field above the texture are shown in Figs. 16(a) and 16(b), respectively. The oscillating components of the field along the CNT are reported in Fig. 16(c).

APPENDIX F: ADDITIONAL INFORMATION ON THE INTERDOT TRANSITIONS DISPERSIONS OF FIG. 4 OF THE MAIN TEXT

1. Magnetic field dependence of the cavity resonant frequency

The Nb resonator resonance frequency shifts with the applied external magnetic field. The magnetic field and frequency dependence of the resonator transmitted microwave signal amplitude is shown in Fig. 17(a), taken simultaneously with the dispersion of the interdot transition ($i_L - i_{L0}, i_R - i_{R0}$) = (1, 1). At a given magnetic field, the frequency is swept at an off resonant point of the interdot transition (large detuning), then the resonance frequency $f(B)$ is extracted and used for the detuning sweep of the interdot transition dispersion measurement. Several background modes are present, which show no dispersion in magnetic field but hinder a precise estimation of the evolution of the cavity line width $\kappa(B)$. We find

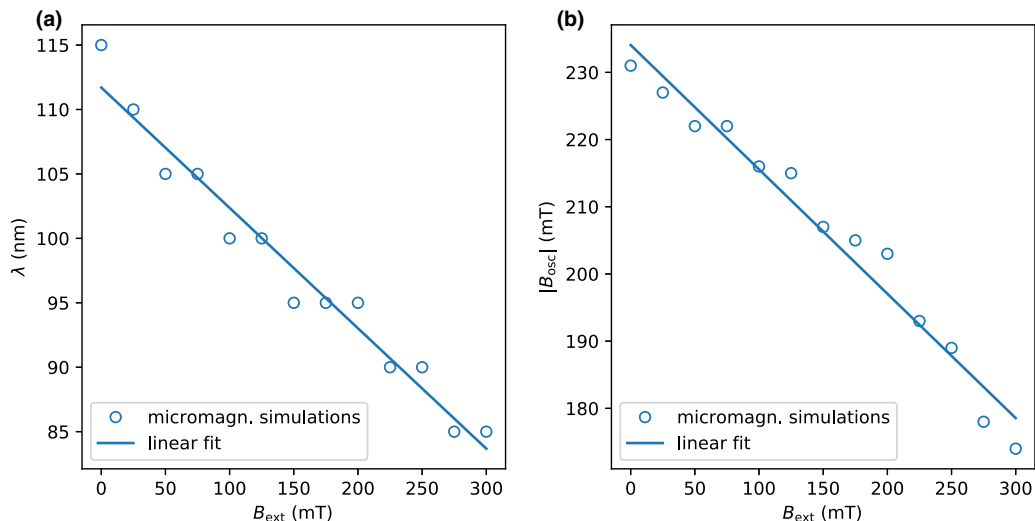


FIG. 15. Simulated field evolution of the cycloidal dipolar stray field. (a) Period λ against external field B_{ext} . (b) Cycloidal field amplitude $|B_{\text{osc}}|$ against external field B_{ext} . In each panel, circles are the micromagnetic simulation points and the line is a linear fit to these points.

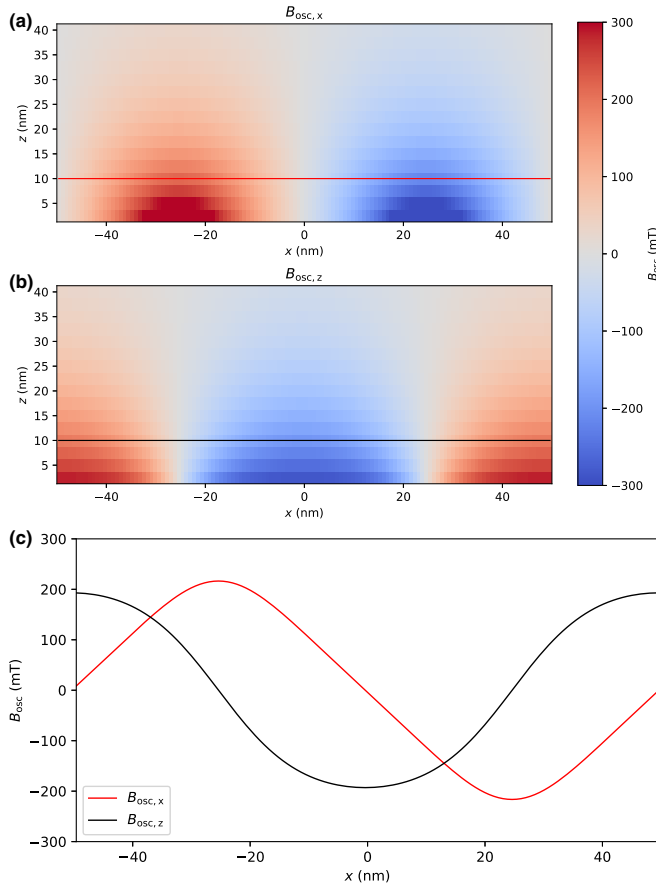


FIG. 16. Cycloidal dipolar stray field generated above CoPt. (a) Spatial evolution of x -component $B_{\text{osc},x}$ above the texture. The red line indicates the cut at $z = 10$ nm (along the CNT) of $B_{\text{osc},x}$ displayed in (c). (b) Spatial evolution of z -component $B_{\text{osc},z}$ above the texture. The black line indicates the cut at $z = 10$ nm (along the CNT) of $B_{\text{osc},z}$ displayed in (c). (c) Cut along the CNT of the two components of the cycloidal dipolar stray field.

that a constant value $\kappa/(2\pi) = 5.5 \pm 0.5$ MHz is appropriate, as the evolution of $\kappa(B)$ is of the order of its uncertainty and its value being 3 to 4 times smaller than the dispersion of f which has negligible effect on the simulation of the signal. Dispersions of the cavity resonance frequency simultaneously acquired with all interdot transition dispersions maps of Fig. 4 of the main text are displayed in Fig. 17(b) showing a robust and reproducible behavior.

2. Summary of the fit parameters of Fig. 4 of the main text

The parameters of the fits for each interdot transitions of Fig. 4 of the main text are presented in Fig. 18 as color coded matrices.

3. Details of each interdot transition dispersion in magnetic field and detuning

In this section, we show detailed analysis of each interdot transition presented in Fig. 4 of the main text. Figures 19–34 of this section presents the B - ϵ/h maps of phase variation $\Delta\phi$ [panels (a) and (b)] (same data and fits as in Fig. 4 of the main text) and amplitude relative variation $\Delta A/A$ [panels (d) and (e)] of the microwave signal, relative to an off value far from the transition. A cut along the resonance condition $\omega_{\text{DQD}} = \omega_{\text{cav}}$, indicated by a red dashed line, is shown for both the data and fits for both $\Delta\phi$ [panel (c)] and $\Delta A/A$ [panel (f)]. Additionally, a cut at fixed B , indicated by an orange dashed line, is shown for both the data and fits for both $\Delta\phi$ [panel (g)] and $\Delta A/A$ [panel (h)]. Finally, a table presenting all the fitting parameters of the given interdot transition is presented [panel (i)].

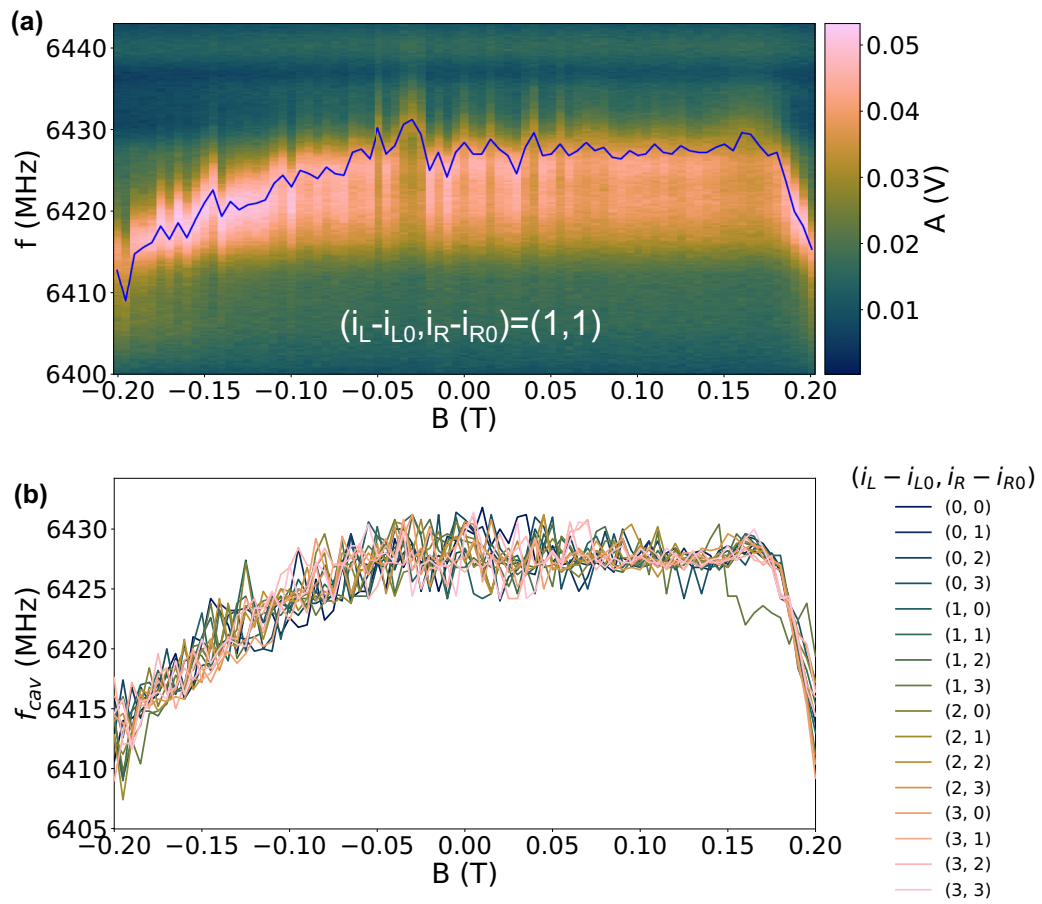


FIG. 17. Magnetic field dependence of the cavity resonant frequency. (a) Magnetic field and frequency map of the microwave signal amplitude simultaneously measured with the dispersion of the interdot transition $(i_L - i_{L0}, i_R - i_{R0}) = (1, 1)$. The position of the resonance frequency is shown as a blue line. (b) Resonance frequency as a function of magnetic field simultaneously acquired with all interdot transition dispersion measurements of Fig. 4.

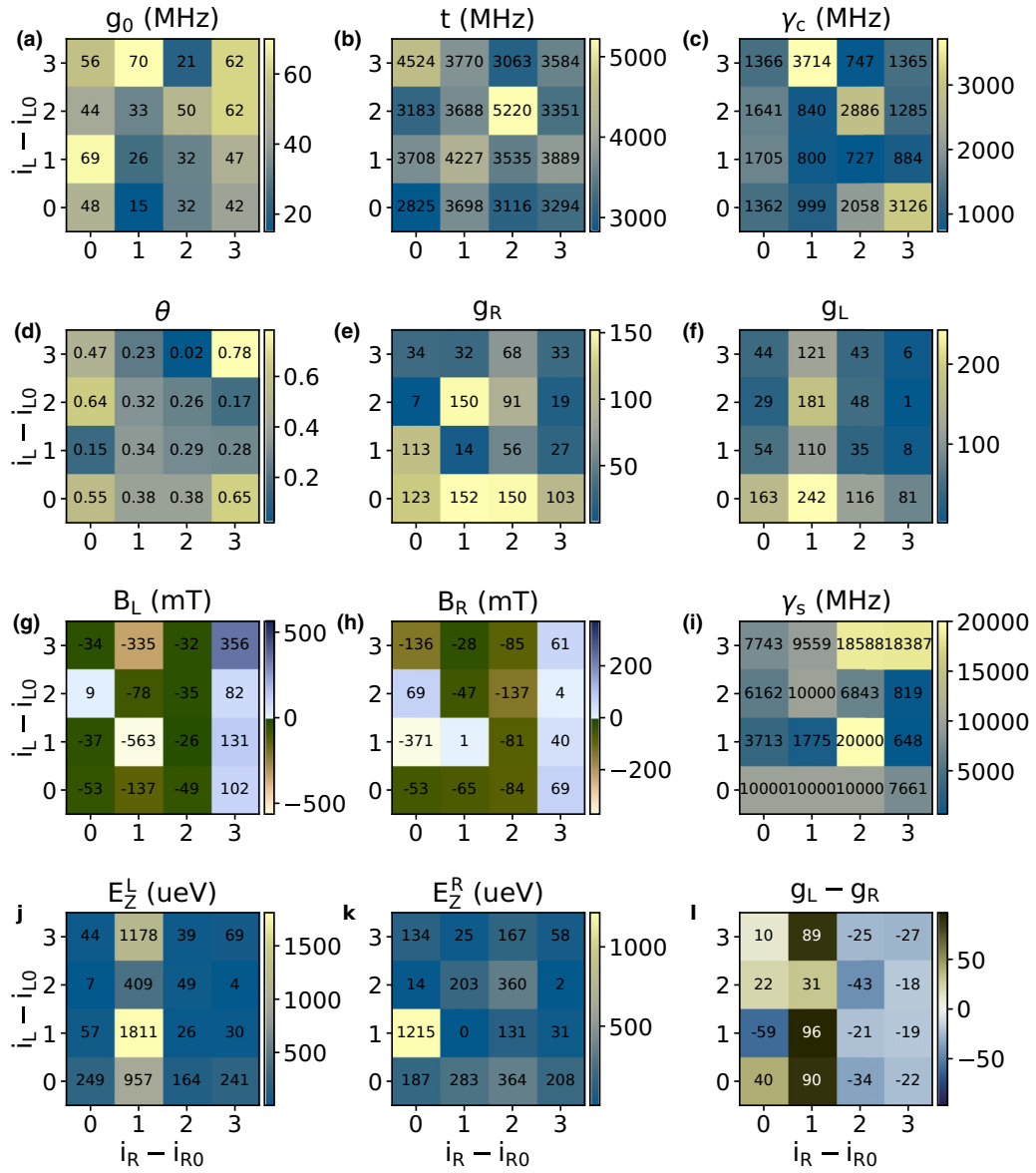
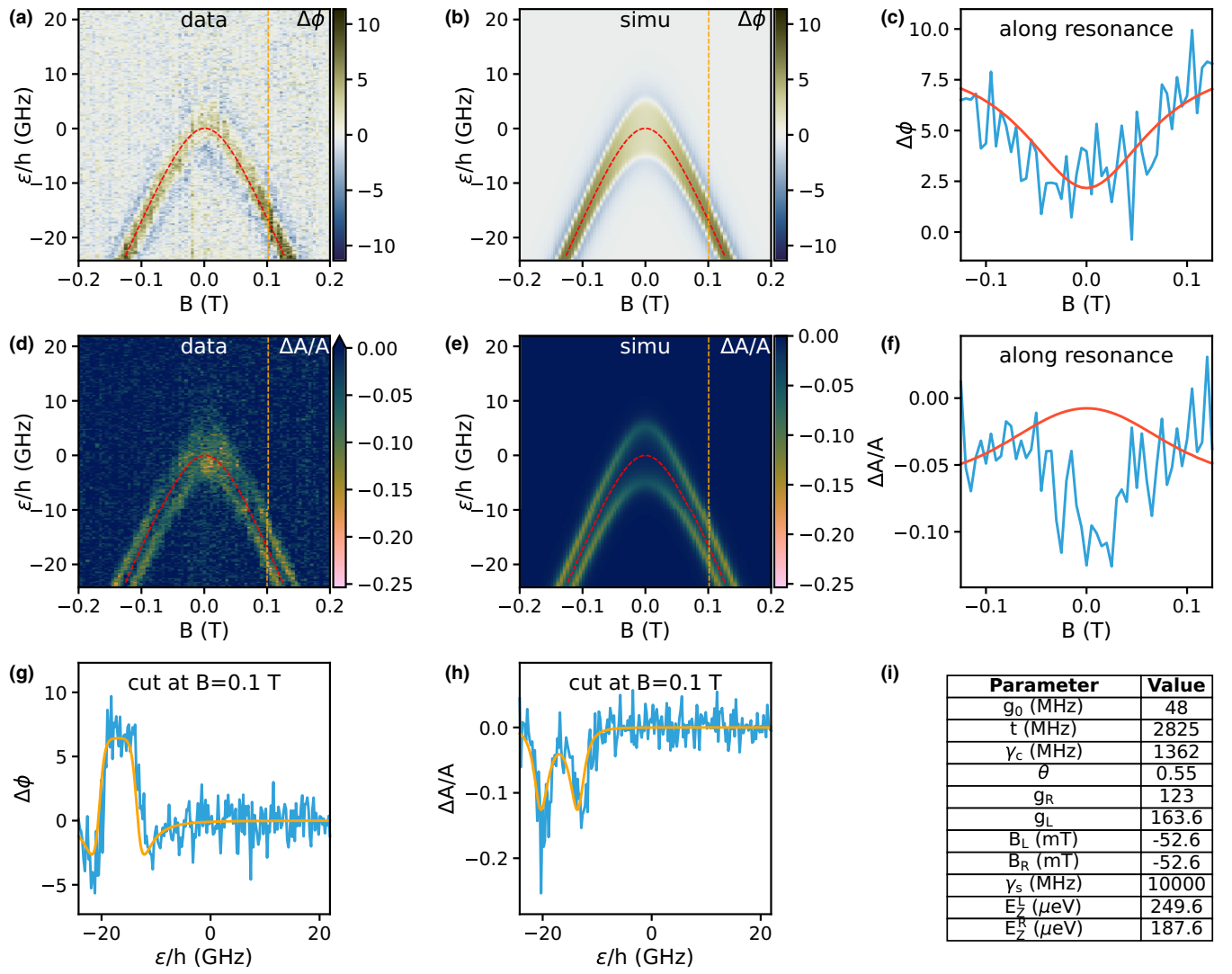
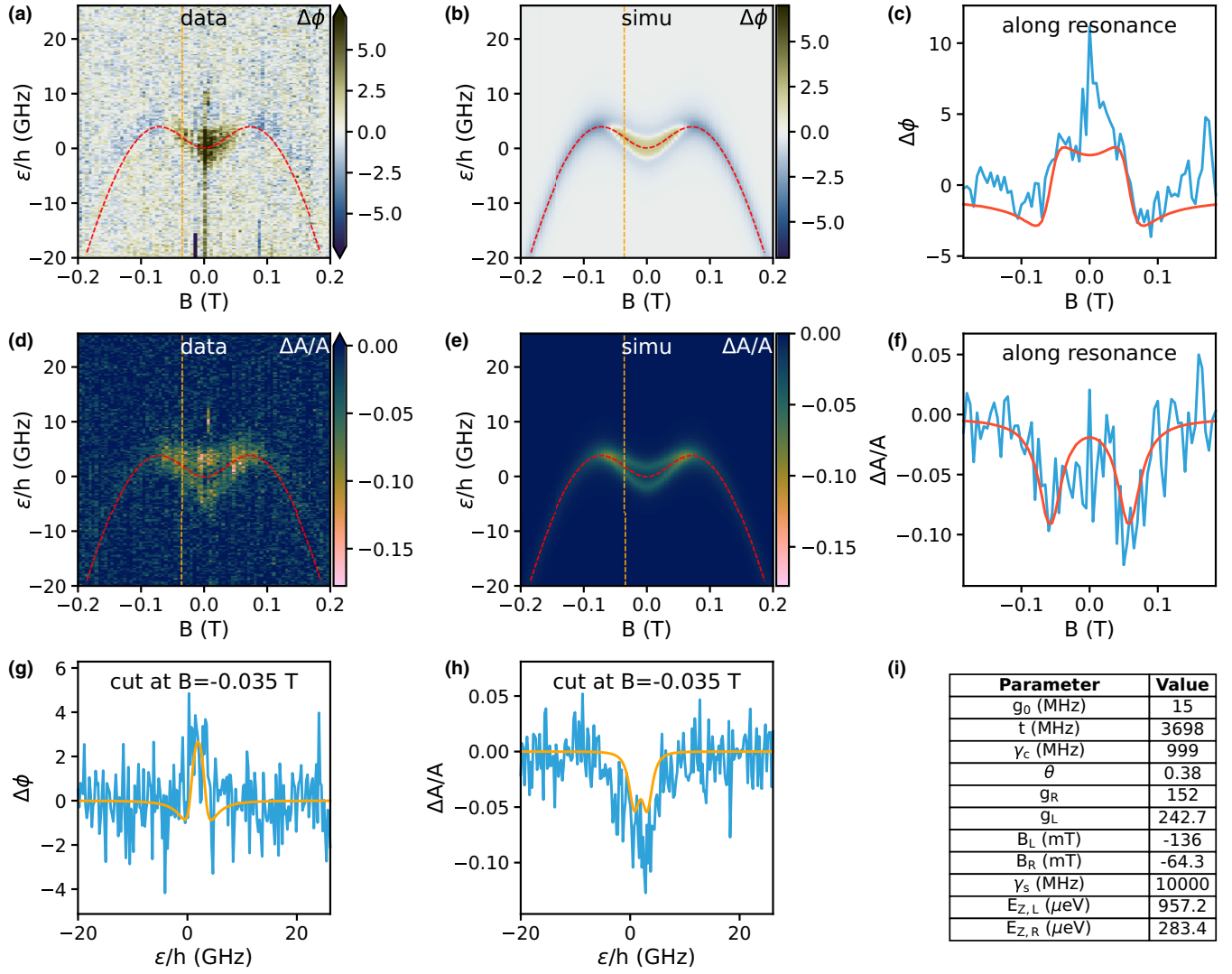


FIG. 18. Fitting parameters. Summary of all the fitting parameters used in Fig. 4(b).


 FIG. 19. Interdot transition (i_{L0} , i_{R0}).

FIG. 20. Interdot transition ($i_{L0}, i_{R0} + 1$).

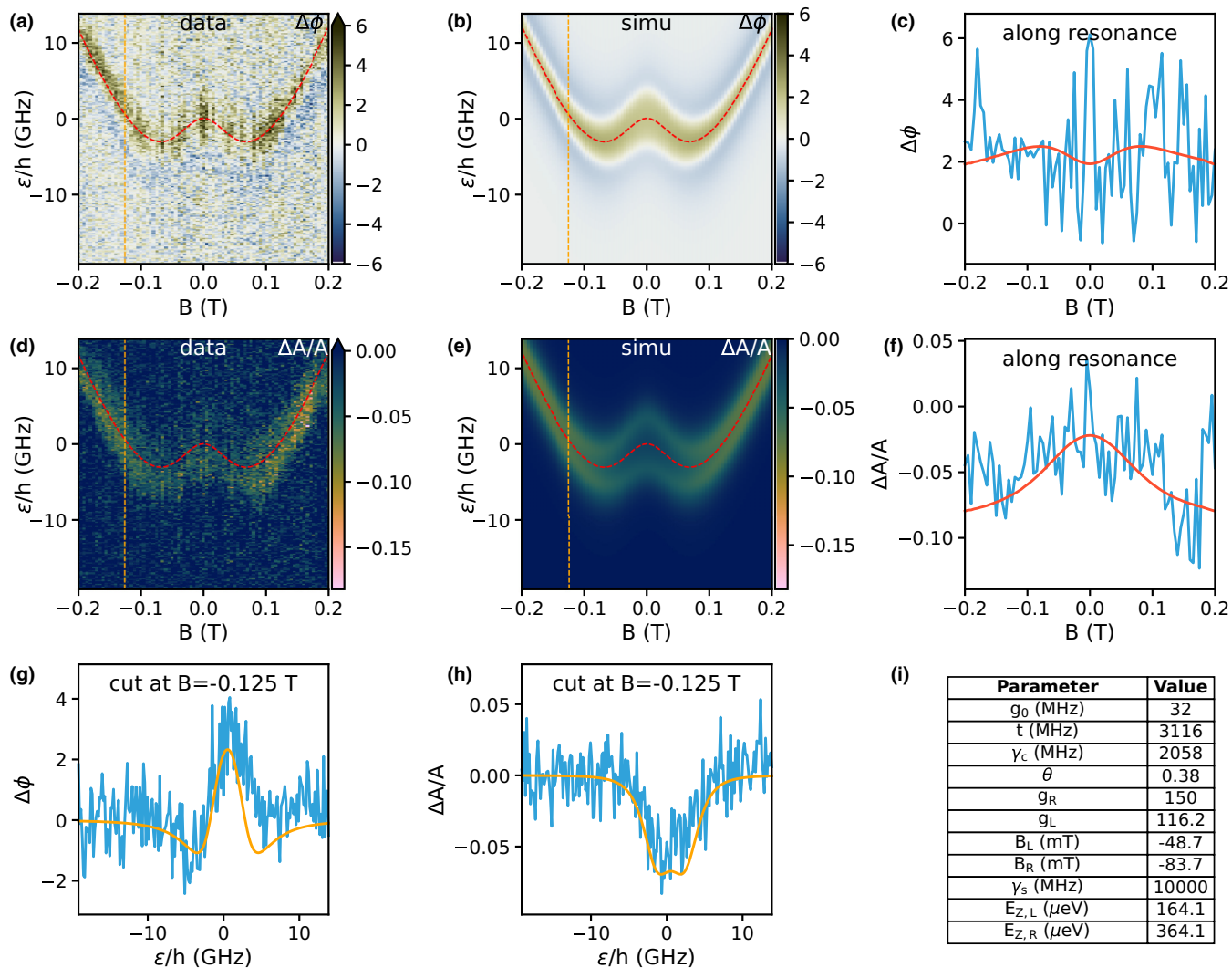
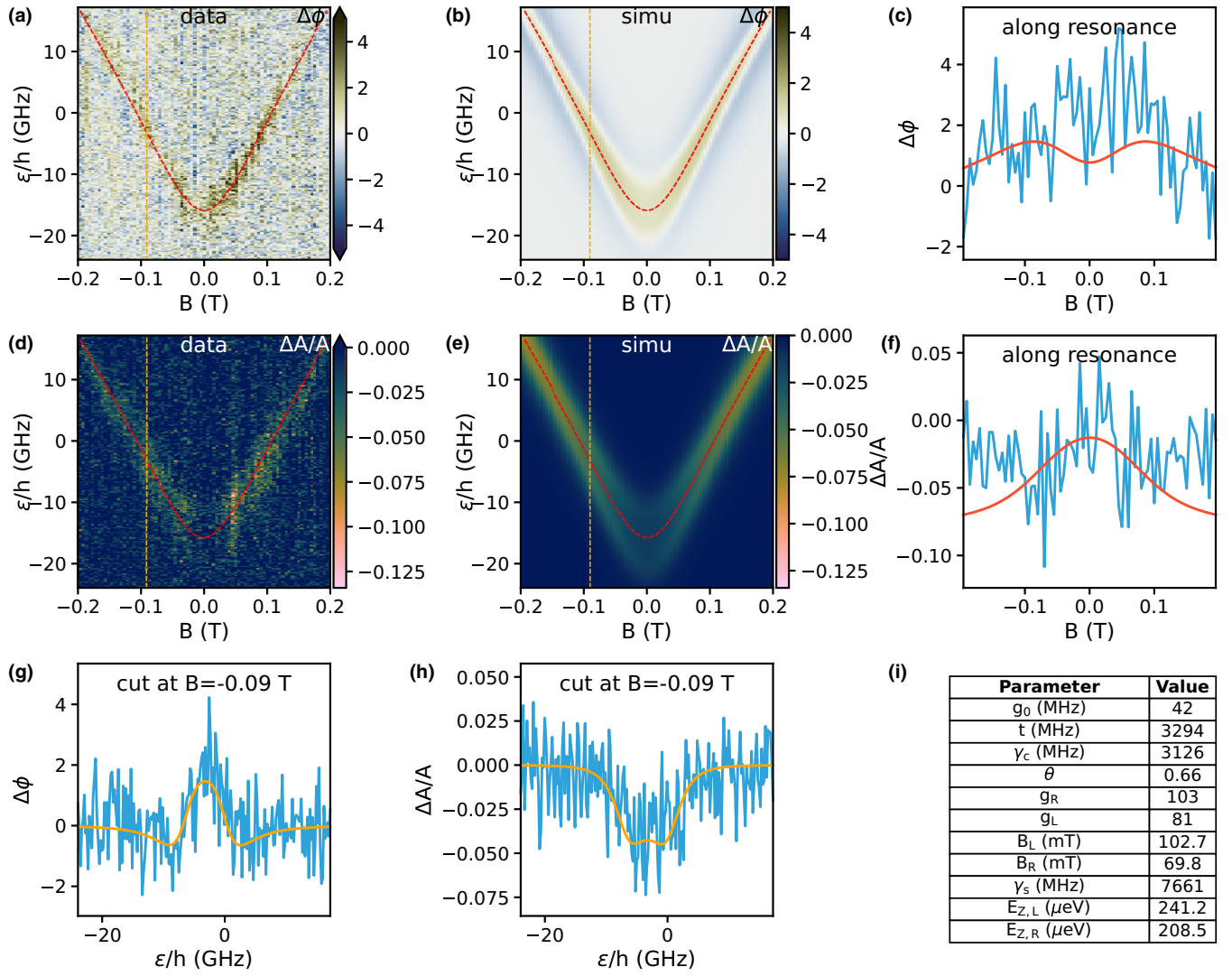
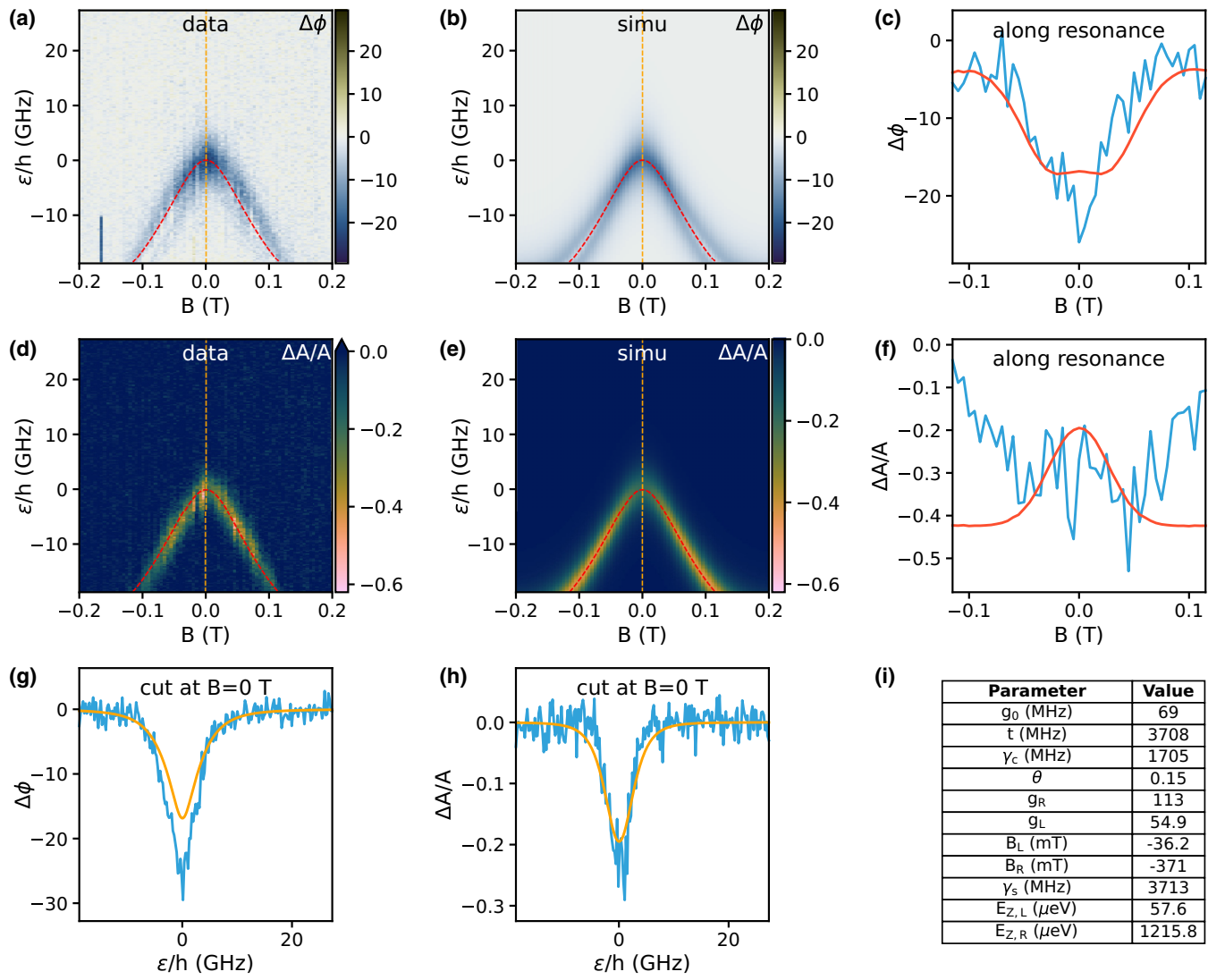
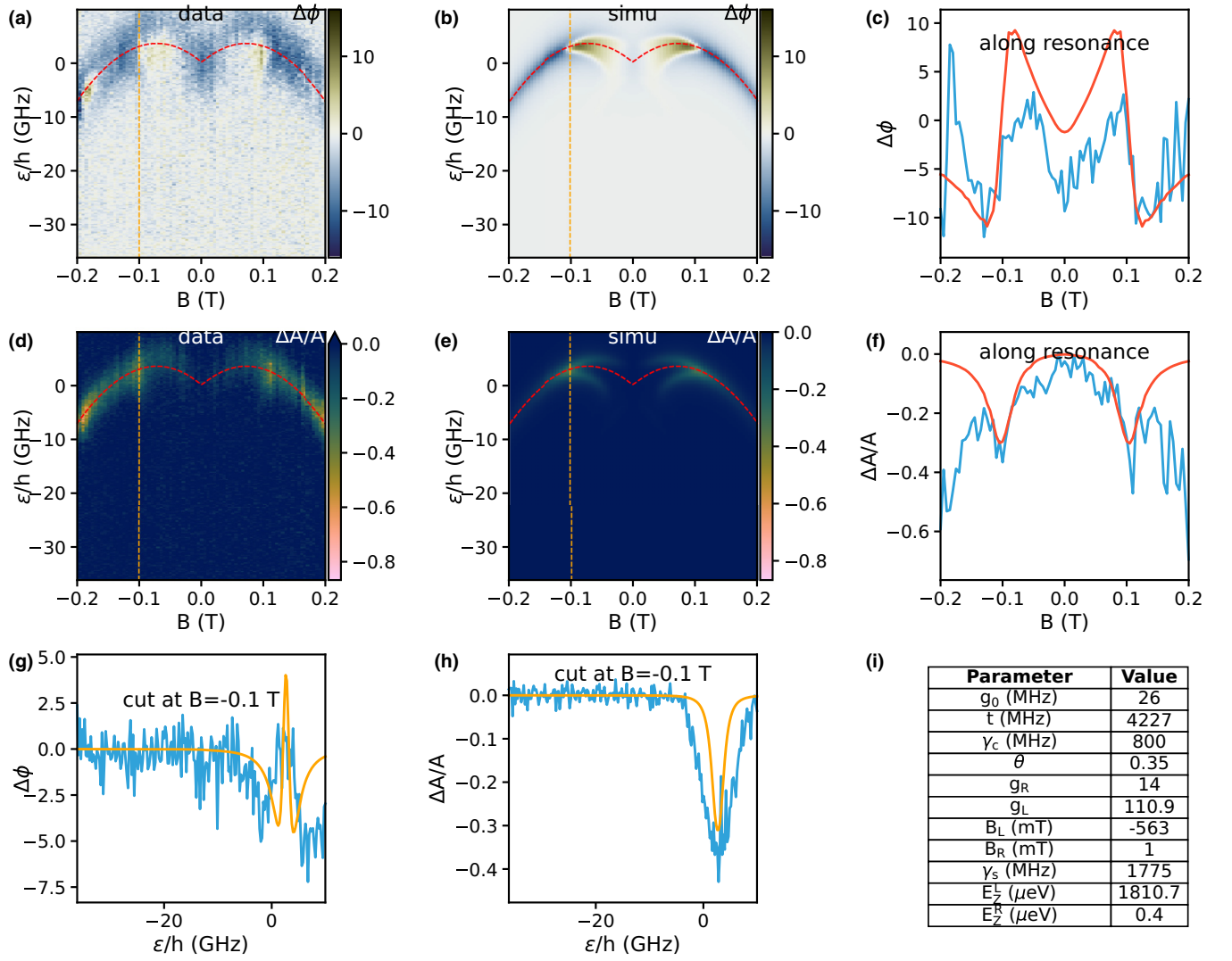
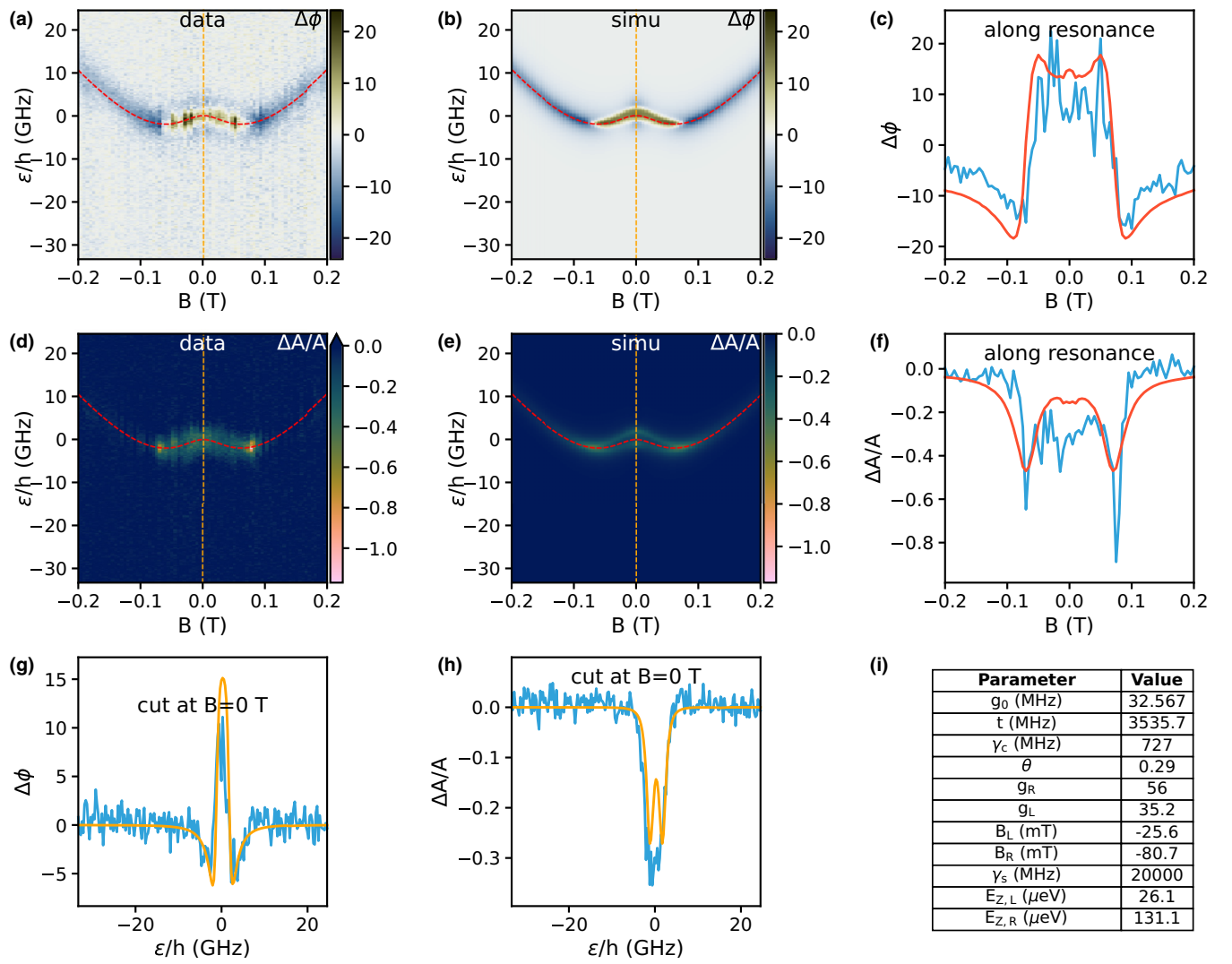


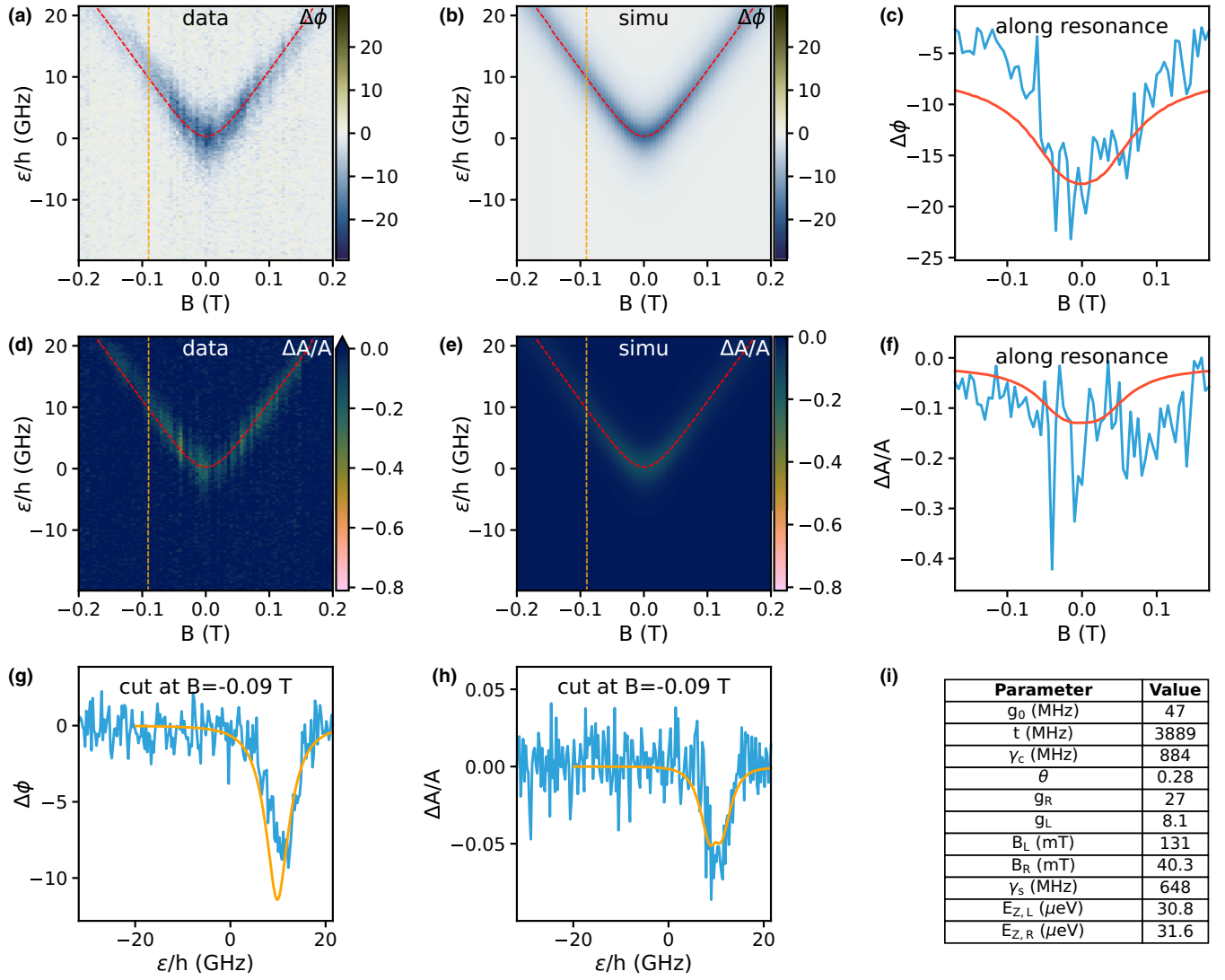
FIG. 21. Interdot transition ($i_{L0}, i_{R0} + 2$).

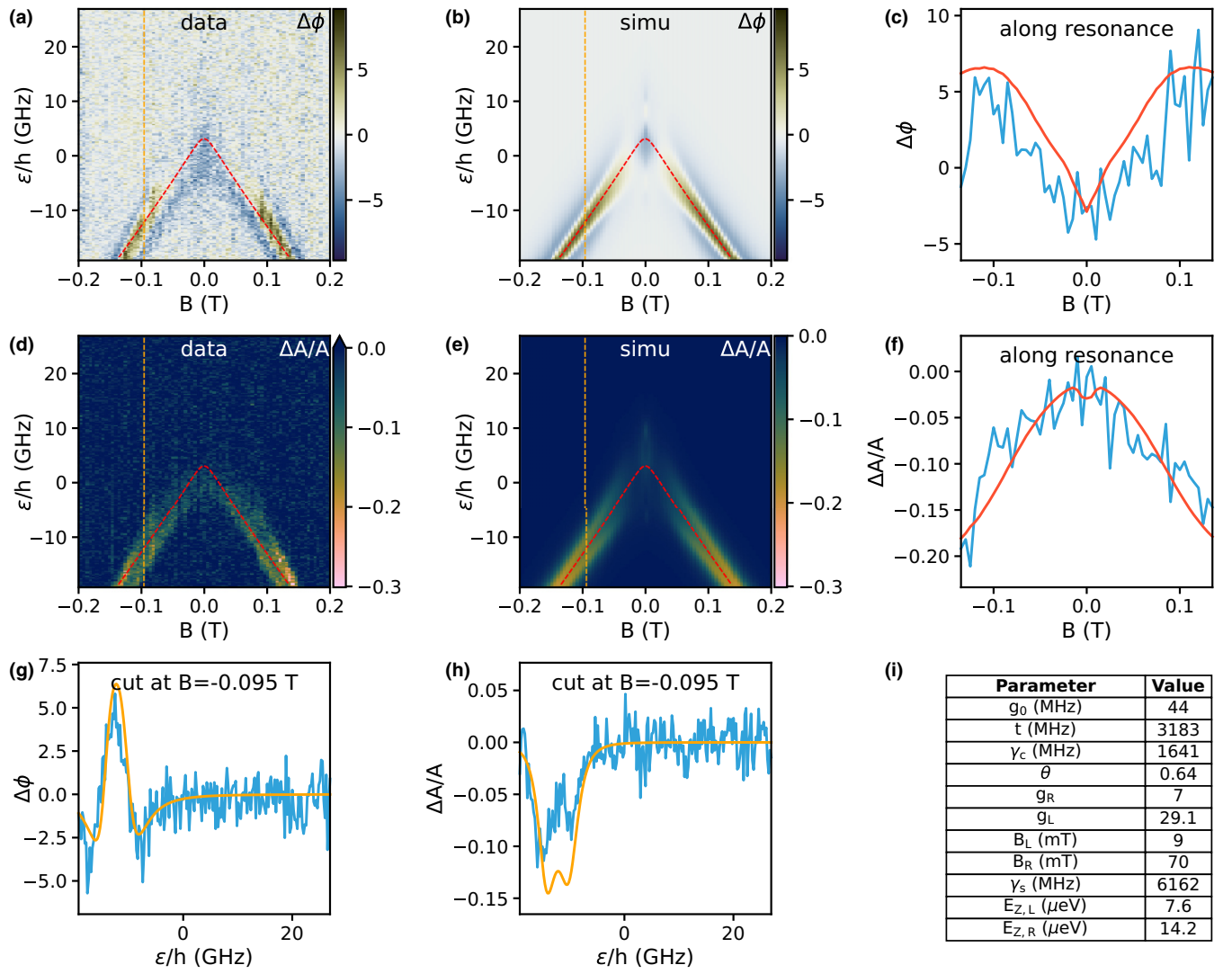
FIG. 22. Interdot transition ($i_{L0}, i_{R0} + 3$).

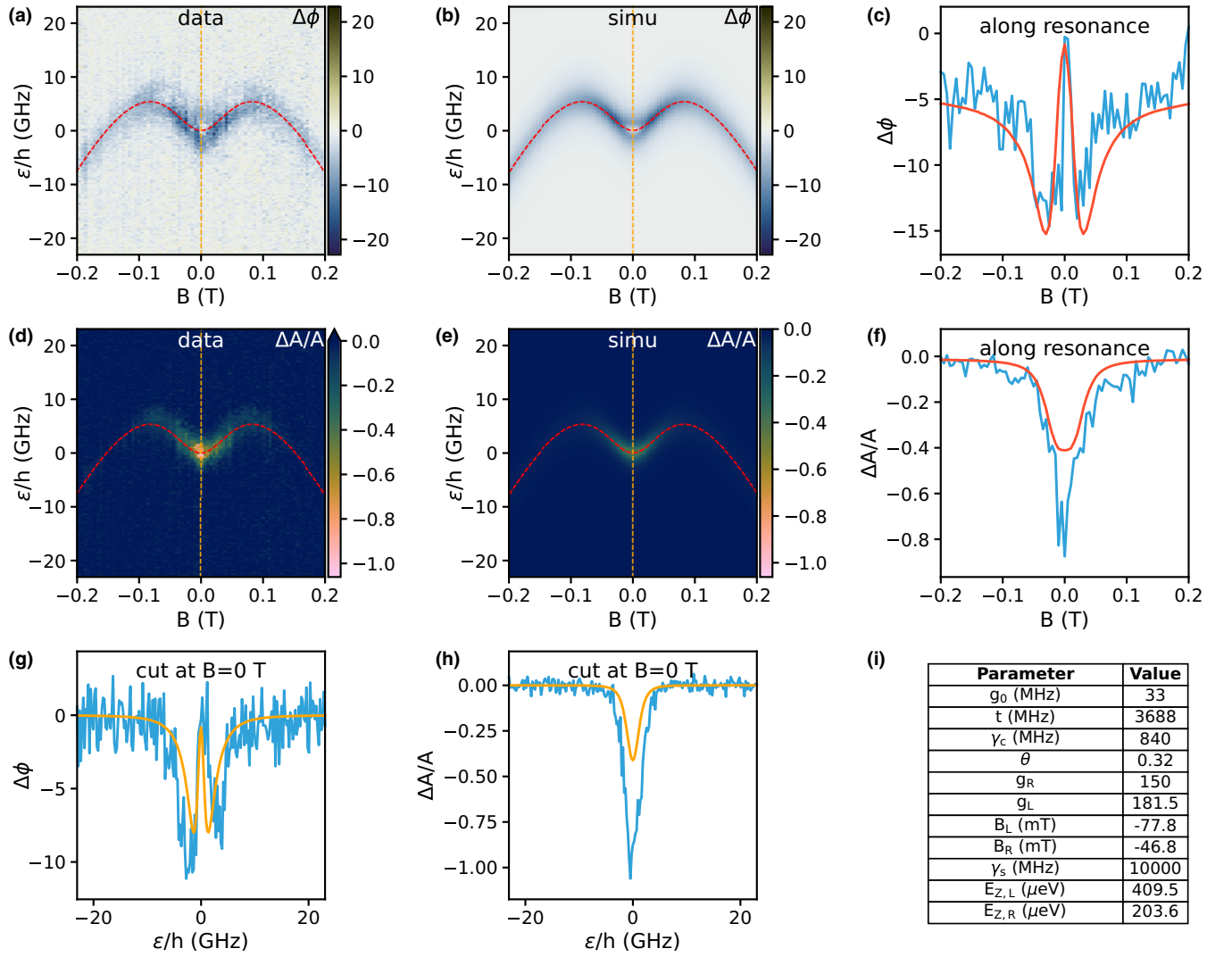

 FIG. 23. Interdot transition ($i_{L0} + 1, i_{R0}$).

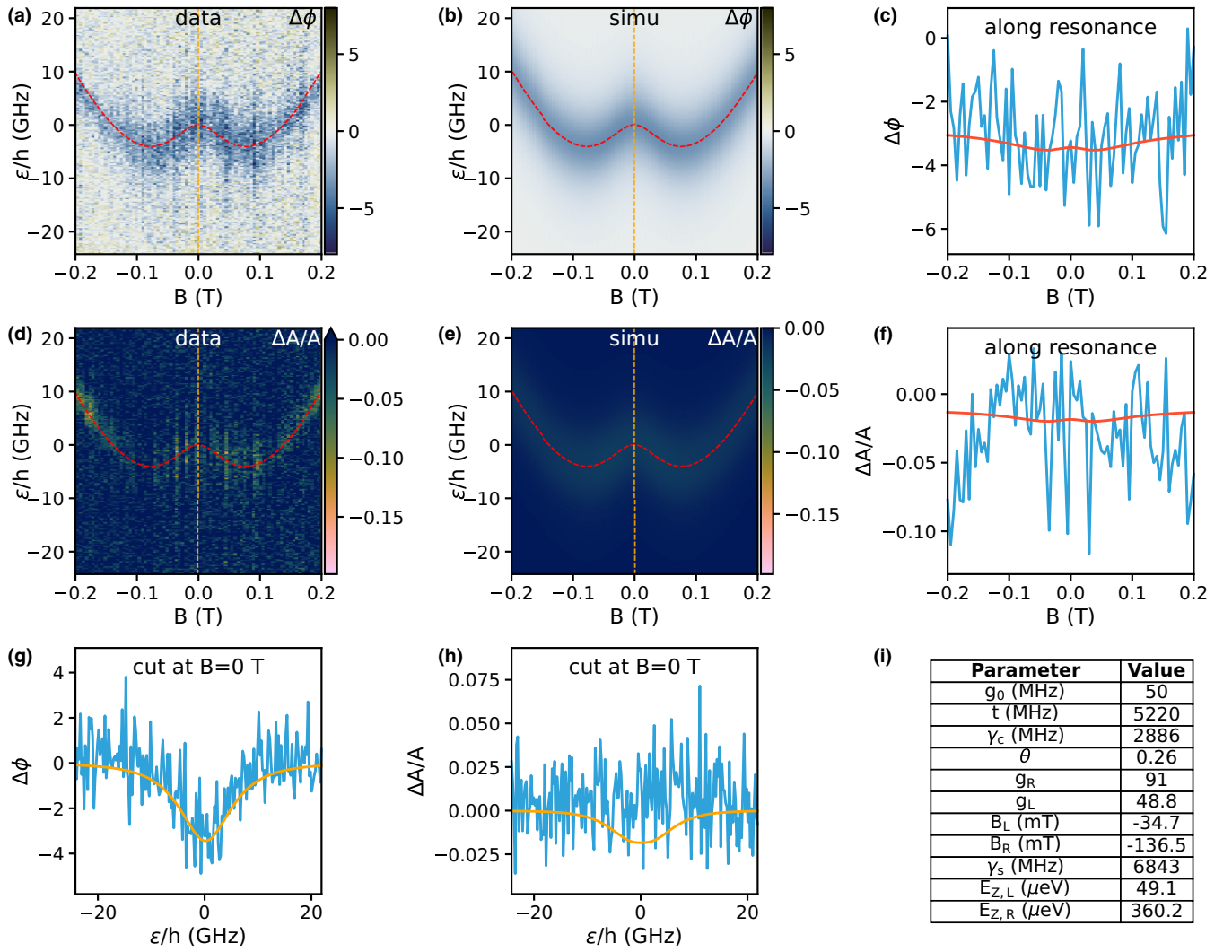
FIG. 24. Interdot transition ($i_{L0} + 1, i_{R0} + 1$).

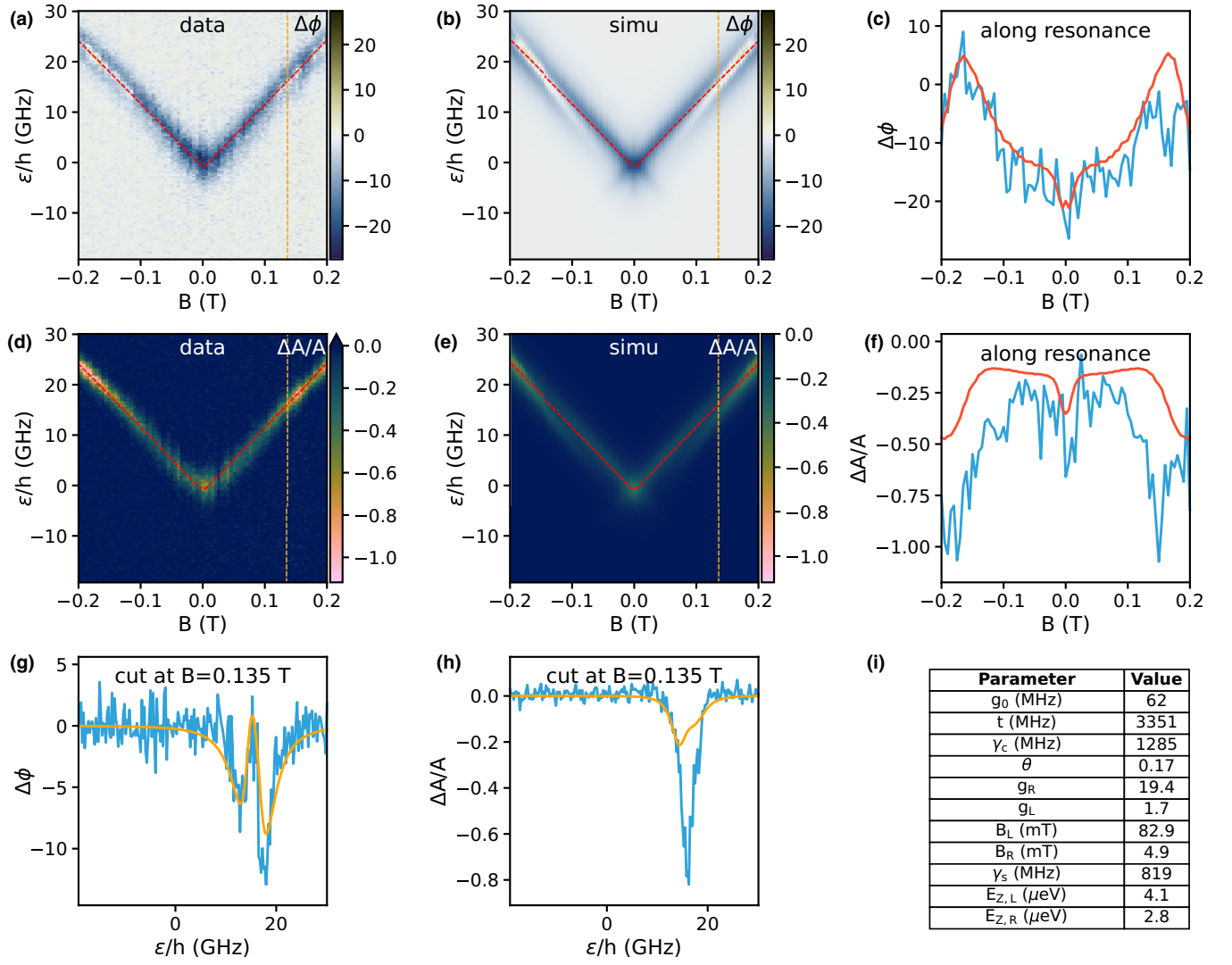

 FIG. 25. Interdot transition ($i_{L0} + 1, i_{R0} + 2$).

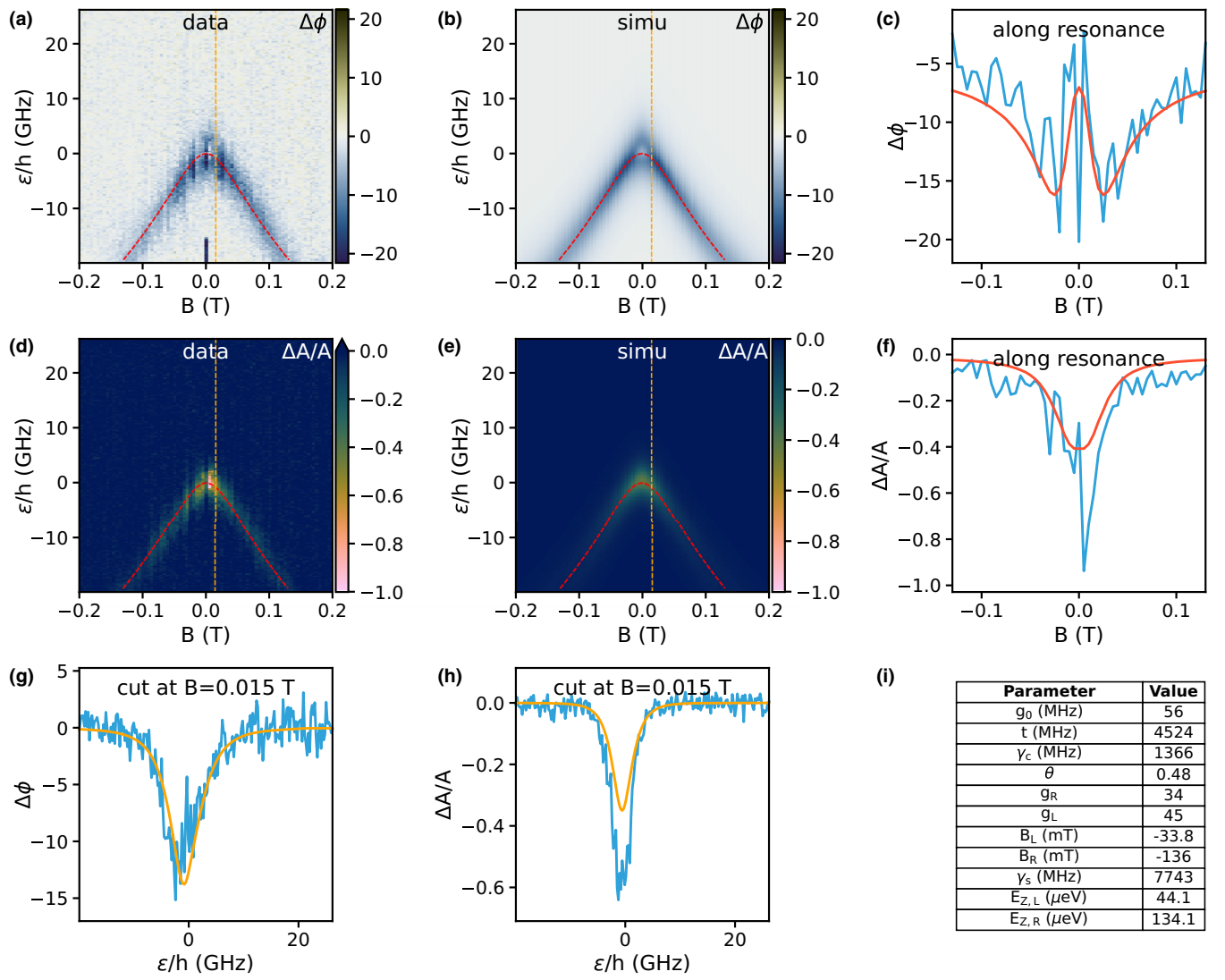
FIG. 26. Interdot transition ($i_{L0} + 1, i_{R0} + 3$).

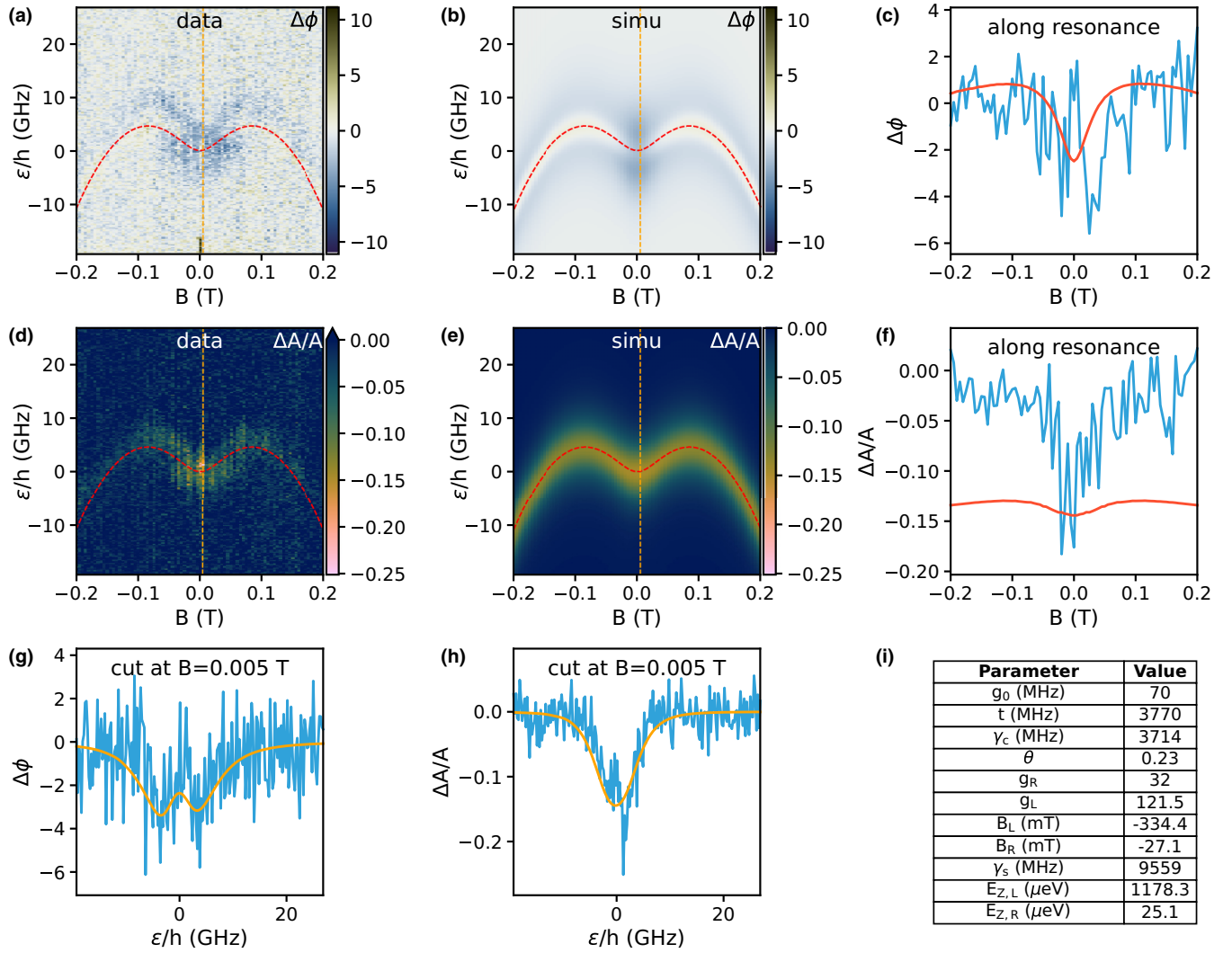

 FIG. 27. Interdot transition ($i_{L0} + 2, i_{R0}$).

FIG. 28. Interdot transition ($i_{L0} + 2, i_{R0} + 1$).


 FIG. 29. Interdot transition ($i_{L0} + 2, i_{R0} + 2$).

FIG. 30. Interdot transition ($i_{L0} + 2, i_{R0} + 3$).


 FIG. 31. Interdot transition ($i_{L0} + 3, i_{R0}$).

FIG. 32. Interdot transition ($i_{L0} + 3, i_{R0} + 1$).

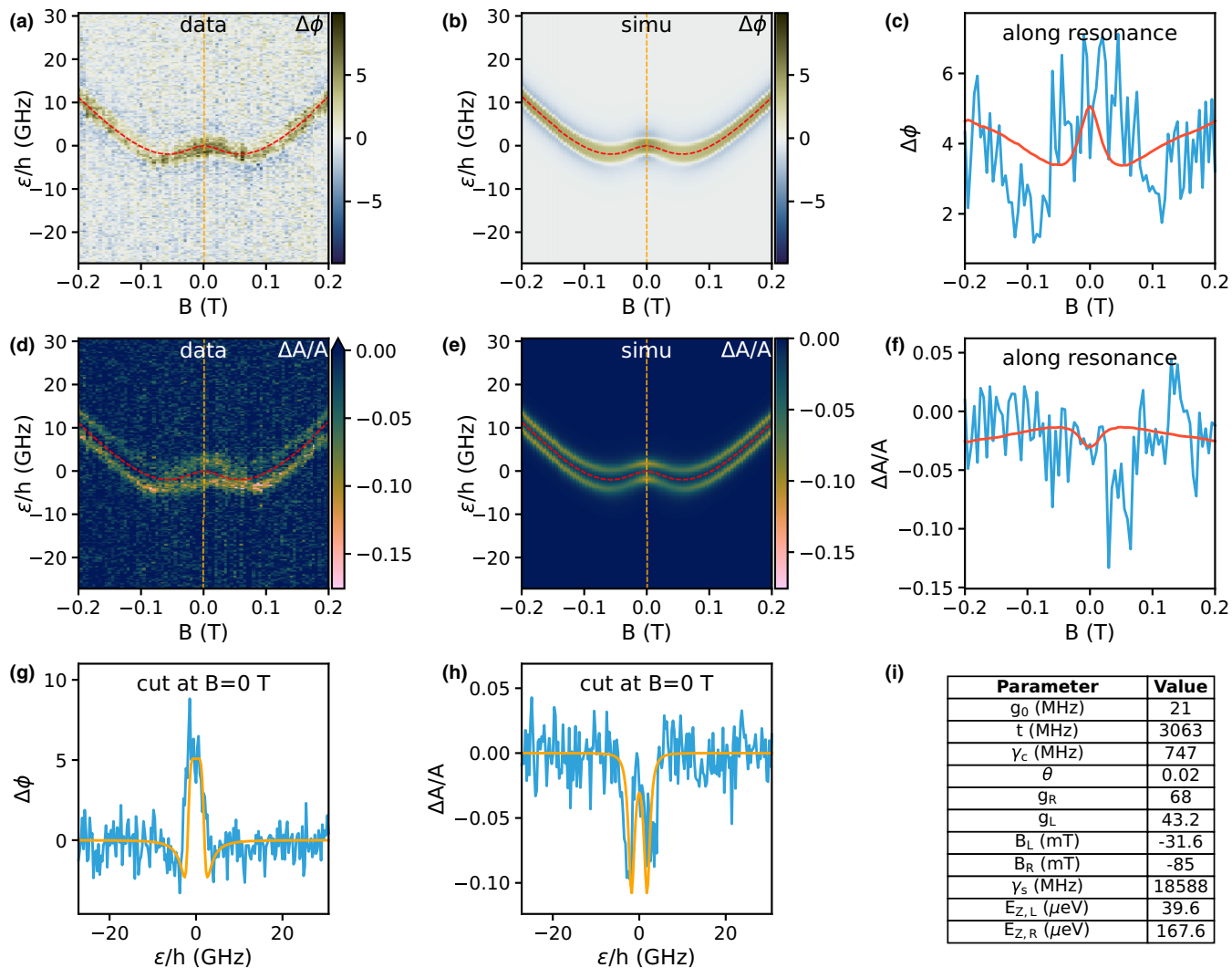
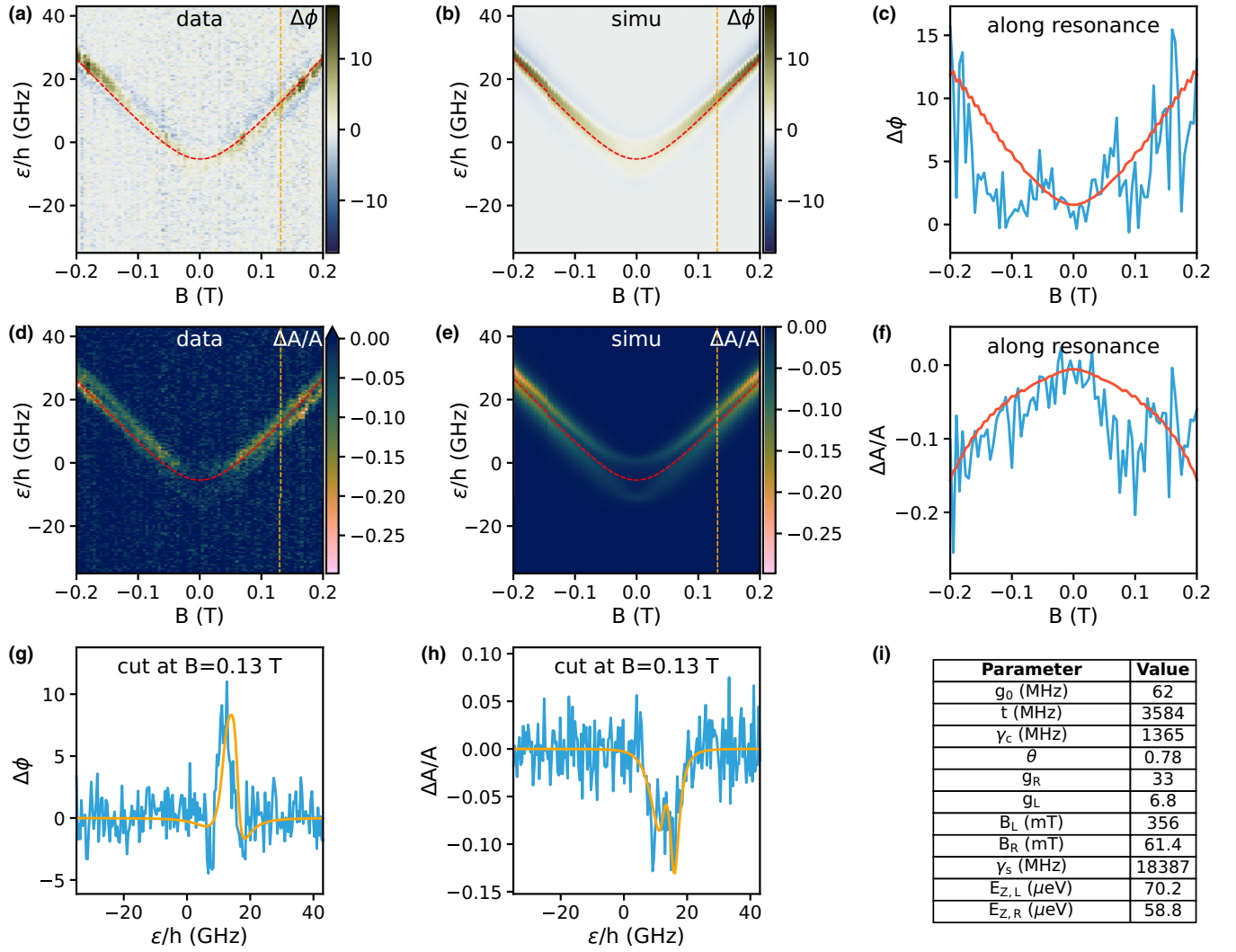


FIG. 33. Interdot transition ($i_{L0} + 3, i_{R0} + 2$).

FIG. 34. Interdot transition ($i_{L0} + 3, i_{R0} + 3$).

- [1] Y. Oreg, G. Refael, and F. von Oppen, *Phys. Rev. Lett.* **105**, 177002 (2010).
- [2] R. M. Lutchyn, J. D. Sau, and S. Das Sarma, *Phys. Rev. Lett.* **105**, 077001 (2010).
- [3] K. Plekhanov, F. Ronetti, D. Loss, and J. Klinovaja, *Phys. Rev. Res.* **2**, 013083 (2020).
- [4] F. Ronetti, K. Plekhanov, D. Loss, and J. Klinovaja, *Phys. Rev. Res.* **2**, 022052(R) (2020).
- [5] J. J. Viennot, M. C. Dartiailh, A. Cottet, and T. Kontos, *Science* **349**, 408 (2015).
- [6] M. M. Desjardins, J. J. Viennot, M. C. Dartiailh, L. E. Bruhat, M. R. Delbecq, M. Lee, M.-S. Choi, A. Cottet, and T. Kontos, *Nature (London)* **545**, 71 (2017).
- [7] M. M. Desjardins, L. C. Contamin, M. R. Delbecq, M. C. Dartiailh, L. E. Bruhat, T. Cubaynes, J. J. Viennot, F. Mallet, S. Rohart, A. Thiaville, A. Cottet, and T. Kontos, *Nat. Mater.* **18**, 1060 (2019).
- [8] C. Kloeffer, M. Trif, P. Stano, and D. Loss, *Phys. Rev. B* **88**, 241405(R) (2013).
- [9] T. Cubaynes, M. R. Delbecq, M. C. Dartiailh, R. Assouly, M. M. Desjardins, L. C. Contamin, L. E. Bruhat, Z. Leghtas, F. Mallet, A. Cottet, and T. Kontos, *npj Quantum Inf.* **5**, 47 (2019).
- [10] J. Klinovaja, P. Stano, and D. Loss, *Phys. Rev. Lett.* **109**, 236801 (2012).
- [11] A. Cottet, M. C. Dartiailh, M. M. Desjardins, T. Cubaynes, L. C. Contamin, M. Delbecq, J. J. Viennot, L. E. Bruhat, B. Douçot, and T. Kontos, *J. Phys.: Condens. Matter* **29**, 433002 (2017).
- [12] D. V. Bulaev and B. Trauzettel, D. Loss, *Phys. Rev. B* **77**, 235301 (2008).
- [13] R. Egger and K. Flensberg, *Phys. Rev. B* **85**, 235462 (2012).
- [14] E. A. Laird, F. Kuemmeth, G. A. Steele, K. Grove-Rasmussen, J. Nygård, K. Flensberg, and L. P. Kouwenhoven, *Rev. Mod. Phys.* **87**, 703 (2015).
- [15] T. Ando, *J. Phys. Soc. Jpn.* **69**, 1757 (2000).
- [16] W. Izumida, K. Sato, and R. Saito, *J. Phys. Soc. Jpn.* **78**, 074707 (2009).
- [17] M. del Valle, M. Margańska, and M. Grifoni, *Phys. Rev. B* **84**, 165427 (2011).
- [18] D. Tománek and S. G. Louie, *Phys. Rev. B* **37**, 8327 (1988).
- [19] C. Sanderson and R. Curtin, *J. Open Source Software* **1**, 26 (2016).
- [20] F. Guinea, C. Tejedor, F. Flores, and E. Louis, *Phys. Rev. B* **28**, 4397 (1983).
- [21] Y. Meir and N. S. Wingreen, *Phys. Rev. Lett.* **68**, 2512 (1992).
- [22] M. Margańska, D. R. Schmid, A. Dirnacher, P. L. Stiller, C. Strunk, M. Grifoni, and A. K. Hüttel, *Phys. Rev. Lett.* **122**, 086802 (2019).
- [23] M. Marganska, P. Chudzinski, and M. Grifoni, *Phys. Rev. B* **92**, 075433 (2015).
- [24] Y. Lu, M. Tran, H. Jaffrès, P. Seneor, C. Deranlot, F. Petroff, J.-M. George, B. Lépine, S. Ababou, and G. Jézéquel, *Phys. Rev. Lett.* **102**, 176801 (2009).
- [25] A. Cottet and T. Kontos, *Phys. Rev. Lett.* **105**, 160502 (2010).
- [26] T. S. Jespersen, K. Grove-Rasmussen, K. Flensberg, J. Paaske, K. Muraki, T. Fujisawa, and J. Nygård, *Phys. Rev. Lett.* **107**, 186802 (2011).
- [27] J. O. Island, M. Ostermann, L. Aspirtarte, E. D. Minot, D. Varsano, E. Molinari, M. Rontani, and G. A. Steele, *Phys. Rev. Lett.* **121**, 127704 (2018).